

Unterschrift des Betreuers



TECHNISCHE
UNIVERSITÄT
WIEN

Vienna University of Technology

DIPLOMARBEIT

Transport of ultracold atoms into a superconducting QulC-Trap

Ausgeführt am Atominstitut
der Technischen Universität Wien

unter der Anleitung von

Univ.Prof. Dr. Hannes-Jörg Schmiedmayer
Univ.Ass. Dr. Stephan Schneider

durch

Christian Novotny

Gruschaplatz 3/10
A-1140 Wien

19. Juli 2011

Unterschrift

Abstract

This thesis describes the setup of an experiment to combine two promising candidates for quantum computation, namely ultra-cold atoms and solid state qubits. Solid state devices, like superconducting coplanar waveguide resonators, can process information very fast but have the disadvantage of very short coherence times. On the other hand, atomic systems like Bose-Einstein condensates provide long coherence times in the order of seconds but are slow in processing. Combining these systems via strong coupling would lead to a fast processing device with long coherence times.

For coupling a cloud of ultra-cold ^{87}Rb atoms to a superconducting microwave resonator, a transport scheme was invented to transport a cloud of ultra-cold atoms into a 4 K-cryostat using a magnetic conveyor belt. Inside the cryostat the atoms were trapped in a superconducting quadrupole-loffé (QulC) trap which allow further cooling to a Bose-Einstein condensate by evaporative radio frequency cooling. During the thesis, parts of the used vacuum chamber were built, coils were manufactured, laser systems for laser cooling in a magneto-optical trap were built and optimized and programs for controlling the experiment were written. Up to 7×10^7 atoms were measured inside the cryostat in a quadrupole trap and were loaded into a quadrupole-loffé trap inside the cryostat for the first time.

Zusammenfassung

Die vorliegende Arbeit beschreibt die Vorbereitungen um zwei vielversprechende Quantencomputer Kandidaten zu vereinen, auf der einen Seite ultra-kalte Atome und andererseits Quantenbits im Festkörper. Solche Festkörper Elemente, wie beispielsweise supraleitende coplanare Wellenleiter Resonatoren, können sehr schnell Information verarbeiten, haben allerdings den Nachteil einer sehr kurzen Kohärenzzeit. Dem gegenüber gestellt haben ultra-kalte Atome bzw. Bose-Einstein Kondensate eine lange Kohärenzzeit von bis zu mehreren Sekunden, sind aber langsam in der Informationsverarbeitung. Durch eine starke Kopplung zwischen diesen Systemen ist es möglich ein Gerät mit schnellem Ansprechverhalten und langer Kohärenzzeit zu realisieren.

Ein magnetischer Transport von Ensembles von Rubidium 87 Atomen ins Innere eines 4 K-Kryostaten wurde entwickelt um die ultra-kalte Atomwolke an einen supraleitenden Mikrowellen Resonator zu koppeln. Im inneren des Kryostaten wurden die Atome in eine Quadrupol-Ioffe Falle geladen, welche ein weiteres Kühlen mittels Verdampfungskühlen und damit Bose-Einstein Kondensation möglich macht. Während dieser Arbeit wurden Teile der verwendeten Vakuum-Aperatur aufgebaut, Spulen wurden geplant und gebaut, das Lasersystem für die Laserkühlung in einer magneto-optischen Falle wurde teilweise aufgebaut und optimiert und Programme für die Experimentsteuerung wurden erstellt. Bis zu 7×10^7 Atome konnten im Kryostaten in einer Quadrupol-Falle nachgewiesen werden und Atome wurden erstmalig in eine Quadrupol-Ioffe Falle im Inneren eines Kryostaten geladen.

Contents

I. The Quantum-Interconnect-Experiment: The motivation	1
1. The motivation	2
II. The Experimental Setup	4
2. Experimental setup	5
3. Basic principles of the magnetic transport	7
3.1. Optical cooling of atoms	7
3.2. Magnetic trapping of atoms	9
3.3. Magnetic transport	10
3.3.1. Current calculations	10
3.3.2. Time calculations	14
3.4. The Quadrupole Ioffe trap	18
3.4.1. Influence of gravitation on the QulC-trap	22
4. Experimental realization	24
4.1. Vacuum Setup and the Cryostat	24
4.1.1. General Setup	24
4.1.2. Compensation Coils	28
4.2. Lasers and Optics	33
4.2.1. Preparing the Laser-Beams	33
4.2.2. MOT- and imaging optics	35
4.3. The MOT cycle	38
4.3.1. MOT and magnetic trap	38
4.3.2. Measurements and optimization	39
4.4. The magnetic transport	46
4.4.1. The normal conducting transport	46
4.4.2. The superconducting transport	47
4.4.3. Superconducting Coils	47
4.4.4. The 4K-cage	53
4.5. Experimental Control	55

4.5.1. The transport currents in ADwin	58
4.5.2. The digital transport channels	59
4.5.3. Sending the data to ADwin	60
III. Results: Atoms in the cryostat	62
5. Results: Atoms in the Cryostat	63
5.1. Atoms in the quadrupole Trap	63
5.2. Atoms in the quadrupole-loffe-trap	69
6. Conclusion and future prospects	70
A. Appendix	72
A.1. Properties of cryogenic materials	72
A.1.1. High purity copper	72
A.1.2. Superconducting wire	73
A.2. Construction plans for the cryo-compensation-coil-mountings	74
B. Acknowledgements	77
Bibliography	78

Part I.

**The
Quantum-Interconnect-Experiment:
The motivation**

1. The motivation

The invention of the laser in 1960 brought, among many other technical devices and scientific applications, a new field of discovering the nature of quantum phenomena. Atoms can be considered as quantum mechanical oscillators with discrete energy levels which can be shifted by the absorption of a photon. Therefore, the laser opened a wide range of possibilities to analyse atomic energy spectra and determine the occurring forces in matter-light interaction. Using this interaction to trap and cool down atoms allowed the development of magneto-optical-traps and led finally to the first Bose-Einstein-condensate (BEC) in 1995 [9, 24]. Based on this milestone in the research of cold quantum gases the technique of magnetic trapping and condensing atoms to a BEC on an atom-chip was possible and was further developed during the following years [25, 34].

Another important field in the research of matter-light interaction is the interaction of atoms with light in an optical cavity described by cavity-quantum-electro-dynamics (CQED) [6]. The cavity can there be described as harmonic oscillator in interaction with a matter wave or BEC, which can be ideally simplified to a two level system. This is one approach for realizing a quantum bit and testing the principles and algorithms for quantum computing, developed throughout the last 30 years [31, 37].

Following the developments and success in CQED experiments, the possibility of realizing a CQED experiment with solid-state devices was investigated. For this field called circuit QED the optical-cavity was replaced by a superconducting transmission line resonator coupled to a superconducting qubit. With this systems coupling strengths could be improved by four orders of magnitude compared to an optical cavity. Another advantage of a transmission line resonator is that it can be coupled to different systems which provide transitions in the microwave regime apart from atoms and molecules. A recent example is the coupling of nitrogen vacancy centers in diamonds to a microwave strip resonator shown in our group [3].

However, the improvement of the coupling strength comes with a smaller coherence time in the order of microseconds compared to several seconds when coupling an atom or molecule to an optical cavity. To compensate this drawback several kinds of *hybrid quantum systems* were proposed [36]. One approach would be to couple a circuit QED system consisting of a transmission line resonator and a charge qubit (Cooper-Pair-Box) to a BEC. It was shown that a cloud of ultra-cold Rubidium 87 atoms trapped near the transmission line resonator could be coupled to the resonator via the hyperfine transition $|F = 1, m_F = -1\rangle \Rightarrow |F = 2, m_F = 1\rangle$. The transition energy corresponds to a microwave photon of 6.83 GHz, which is ideally suited for a

transmission line resonator. With a postulated quality factor of $Q \approx 10^6$ and about 10^6 ultracold atoms, it was shown that coherence times of more than 1 s could be achieved [32, 40]. In our lab we were recently able to measure a high quality factor of 10^6 in the experiment.

The quantum-interconnect experiment aims on realizing the described theoretic concept. To achieve a hybrid quantum system one would have to bring ultracold atoms in a cryogenic environment at below the critical temperature of the superconductor ($T_C = 9.2$ K in case of Niobium). To trap atoms in a magneto-optical-trap in such a cryogenic environment, one can not use thermal evaporation of rubidium to provide the atoms because of heat dissipation at the dispenser. An alternative non thermal evaporation method for ^{87}Rb with an electron beam was investigated but led to the result that the number of evaporated atoms is too low for trapping and cooling down to a BEC [19].

Therefore we chose the different approach of trapping the rubidium atoms in a magneto-optical-trap at room temperature and transporting them afterwards into a 4 K-cryostat. Two transport schemes were investigated, a laser driven transport in an optical lattice and a magnetic transport with a shifted magnetic quadrupole trap. Results of calculations showed that the second option is the favorable one [27].

Inside the cryostat we follow two possibilities to reach Bose-Einstein-condensation of the atoms. As first possibility we implemented a quadrupole-Ioffe-trap (QulC-trap) inside the cryostat to load atoms into a harmonic trap potential which allows cooling to a BEC by evaporative radio frequency cooling [15] and finally coupling to a transmission line resonator made from Niobium. As second option an Atom-Chip with a superconducting Z-shaped wire trap configuration can be mounted inside the cryostat near a transmission line resonator. The atoms can be loaded into the Z-trap and condensed to a BEC by evaporative cooling [35]. The advantages of a superconducting atom-chip are amongst others a low noise level and longer lifetimes for the trapped atoms [22].

The cryostat works as a cryopump and therefore the time to reach a descent vacuum is in the order of hours compared to weeks in a common room temperature experiment. Additionally, our modular design allows to open the cryo chamber without changing other experimental devices such as the optics. Due to these factors we reach a turn around time of our experiment of only one to two days while the turn around time for a room temperature experiment is a few months. This is a big advantage of an optical experiment in a cryogenic environment.

In this thesis I describe a new constructed experimental setup to transport ultracold ^{87}Rb atoms with a magnetic conveyor belt into a cryostat and trapping and measuring atoms inside the cryostat in a QulC-trap.

Part II.

The Experimental Setup

2. Experimental setup

Fig.(2.1) shows a schematic of the experiment. Details about the vacuum chamber and the setup of the cryostat are given in Section 4.1. To transport atoms into a 4K cryostat we follow several steps. For trapping atoms in a magneto-optical trap in the MOT chamber we need to prepare lasers for the laser cooling process and built an optical setup to provide the laser beams, this is described in detail in Section 4.2. To achieve a MOT and trap atoms in a magnetic trap we need an exact timing of laser light and magnetic fields, the theory behind this is described in Section 3.1, while the experimental details and measurements to optimize the MOT are discussed in Section 4.3.

After trapping the atoms in a magnetic quadrupole trap inside the MOT chamber, we use a magnetic conveyor belt to transport the atom cloud first horizontally underneath the cryostat and then vertically by using superconducting transport coils. The theoretic considerations and calculations are given in Section 3.3, while Section 4.4 shows the implementation in the experiment.

We use digital and analog signals to control the magnetic transport and other experimental processes provided by a commercial ADwin system which runs on a windows XP PC and is controlled via a matlab¹ programming surface. Section 4.5 shows some programming details considering the magnetic transport.

We were able to transport more than 7×10^7 atoms into the cryostat and hold them in a quadrupole trap. Section 5.1 gives measurements and characteristics of atoms in the cryostat.

We also accomplished the loading of atoms into a quadrupole-loffe trap. Section 3.4 shows the theoretical considerations regarding a so called QuIC trap while Section 5.2 gives first pictures and results of trapped atoms.

¹MathWorks matlab 7.9.0

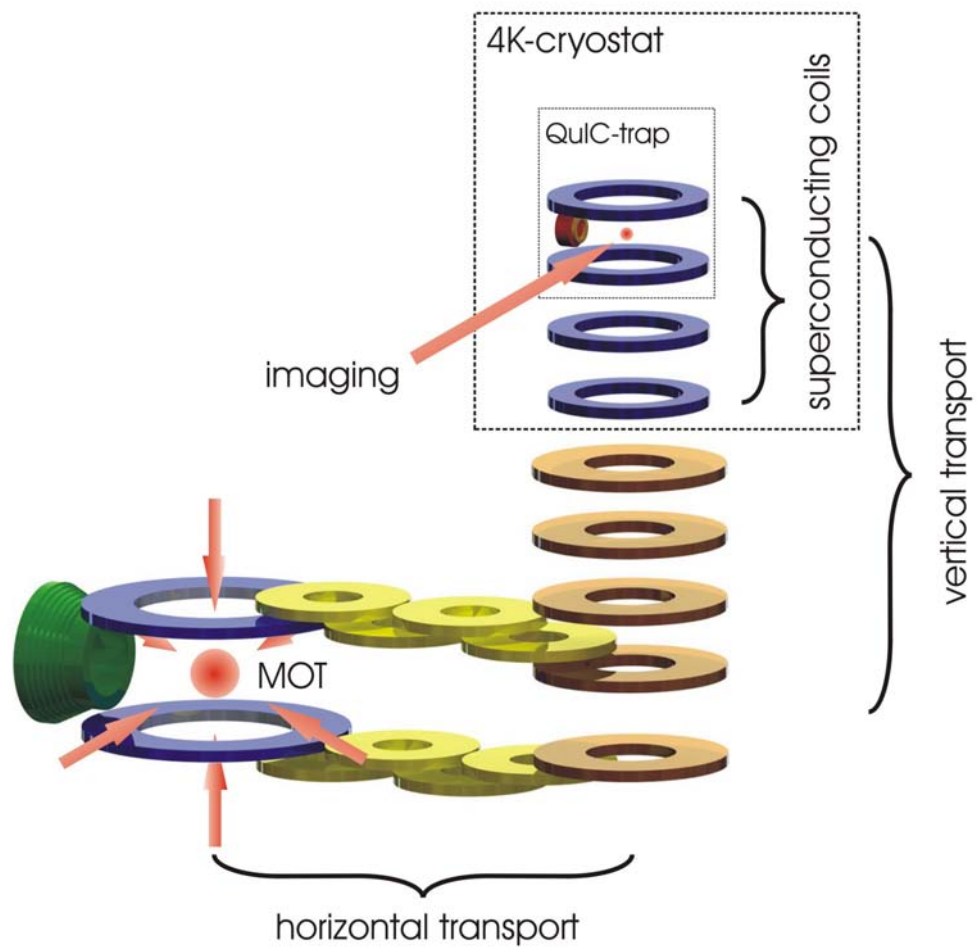


Figure 2.1.: Main elements of the quantum interconnect experiment

3. Basic principles of the magnetic transport

3.1. Optical cooling of atoms

The first step for transporting ^{87}Rb atoms into the cryostat is trapping and cooling the atoms in a magneto-optical trap (MOT). Our MOT consists of 6 circular polarized counter propagating laser beams pointing on the center of the MOT chamber and two MOT coils which are operated in anti-Helmholtz-configuration. These coils produce a quadrupole magnetic field, which absolute value is zero at the MOT center and has a constant gradient in each direction [5]. The gradient is inducing a position dependent Zeeman splitting in the hyperfine structure of Rb87 atoms (Fig.(3.1)). To trap the atoms in the center, one uses a laser which is a few MHz red-detuned from the atomic resonance so the atoms are on resonance at a certain distance from the center. Then they can absorb a photon, which has the right polarization depending on the selection rules. This condition is met by the beam propagating into the center¹. The atoms get an impulse in direction of the center by photon induced excitation and fall back to the ground state by emitting a photon in an arbitrary statistical direction. This results in the movement towards the center of the trap. Since this is the case in all three special directions the atoms get trapped in a certain volume, determined by the coil current and the laser detuning. This momentum transfer has also a cooling effect, which is limited by the power broadening of the laser and the Doppler broadening of the transition line. Therefore, the lowest reachable temperature in a MOT is called Doppler limit [15]. It depends on the natural linewidth $\Gamma_{^{87}\text{Rb}} = 2\pi \cdot 6.065\text{MHz}$ of rubidium and can be calculated to $T_D = \frac{h}{4\pi k_B} \Gamma = 145.5 \mu\text{K}$ [35].

Fig.(3.1) shows the level scheme of ^{87}Rb . The transition used for cooling, trapping and finally imaging is $5^2S_{1/2} | F = 2 \rangle$ to $5^2P_{3/2} | F = 3 \rangle$. Since ^{87}Rb is no ideal two-level system, there is the possibility that atoms are excited to the $5^2P_{3/2} | F = 2 \rangle$ state and decay into the $5^2S_{1/2} | F = 1 \rangle$ state. This is a dark state for the cooling light and therefore the atoms would fall out of the trapping/cooling cycle. To prevent this, an additional re-pumping laser, tuned on the transition $5^2S_{1/2} | F = 1 \rangle$ to $5^2P_{3/2} | F = 2 \rangle$, is overlaid with the cooling beam.

After collecting and cooling atoms in the MOT for some time (refer to Section 4.3 for

¹Two counter propagating beams are polarized circular (σ^+ and σ^-) in respect to the atoms

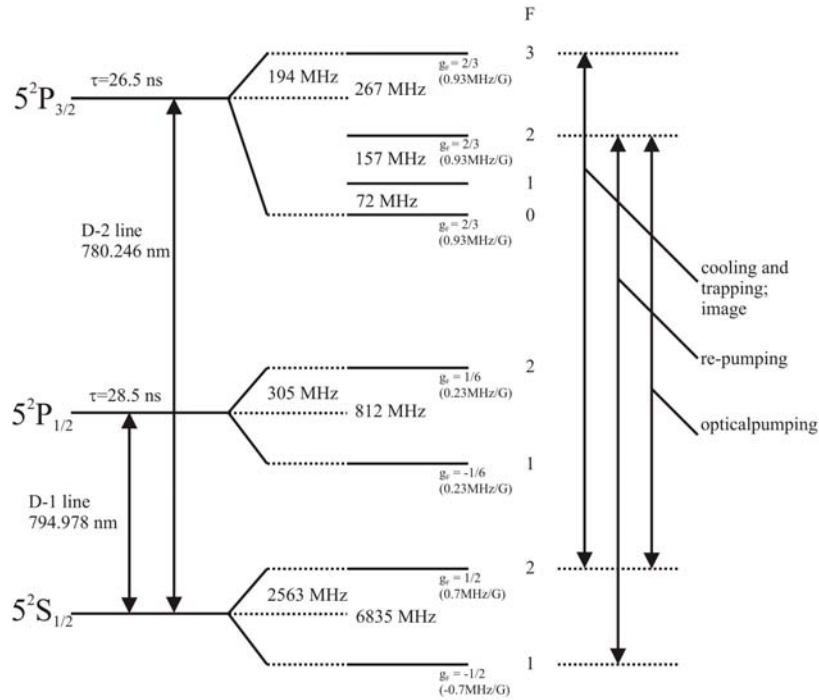


Figure 3.1.: Energy levels of Rubidium 87

used durations and achieved atom numbers) we apply additional cooling in an optical molasses to reach temperatures below the Doppler limit (Sub-Doppler cooling). For the optical molasses the MOT coil current is set to zero and the laser beams are detuned to a few MHz lower frequency than the cooling frequency. Dalibard et al. [8] describe Sub-Doppler cooling in the $\sigma^+ - \sigma^-$ configuration as a mechanism called *motion-induced orientation*. Two counter-propagating circular polarized laser beams form a beam in which the polarization changes depending on the position on the beam axis (as sketched in Figure 3.2). Since transition-probabilities vary with the polarization (*Clebsch-Gordon-Coefficients*), this polarization gradient leads to an unbalance of the transition probabilities that slows the atoms down.

For imaging atoms in the MOT chamber and after the transport in the cryostat we send resonant laser light through the chamber on a CCD chip. The atoms absorb the light, therefore areas with atoms drop a shadow and have lower intensity on the picture. By calculating the relative intensity between one picture with atoms and a picture of the laser beam without atoms, one can derive among other parameters the atom number and the shape of the cloud. This procedure is called absorption imaging [12, 33].

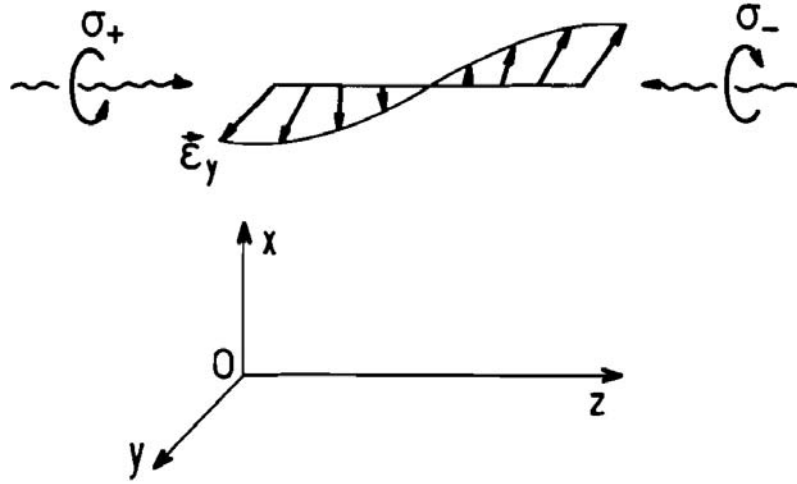


Figure 3.2.: Sketch for sub-Doppler cooling in the molasses, taken from [8].

3.2. Magnetic trapping of atoms

After the molasses step we need to trap the atoms in a pure magnetic trap to make them ready to be transported. Wings theorem [42] states that it is impossible to produce a local maximum of the magnetic field in a *region devoid of charges and currents*, like a neutral gas or vacuum. Therefore most magnetic traps use a field minimum to trap the atoms, so does a quadrupole trap. For being trapped in a quadrupole trap atoms need to be in a low-field seeking state, which means the energy of the atom is direct proportional to the strength of the magnetic field. The Zeeman energy is calculated by $E = \vec{\mu} \vec{B} = g_F m_F \mu_B |\vec{B}|$, the condition for a low field seeking state is

$$g_F m_F \geq 0 \quad (3.1)$$

If this is the case, the atoms will stay in the center of the trap where the magnetic field is zero and the energy is minimized.

For ^{87}Rb the states $5^2S_{1/2} | F = 1, m_F = -1 \rangle$, $5^2S_{1/2} | F = 2, m_F = 1 \rangle$ and $5^2S_{1/2} | F = 2, m_F = 2 \rangle$ are low-field-seeking. The third state experiences a twice as strong force due to a magnetic gradient compared to the other two, and therefore we use this state to trap and transport the atoms. With an optical pumping step after the molasses (shown in Fig.(3.1)) we can bring the atoms to the desired state by using the $5^2S_{1/2} | F = 2 \rangle \Rightarrow 5^2P_{3/2} | F = 2 \rangle$ transition.

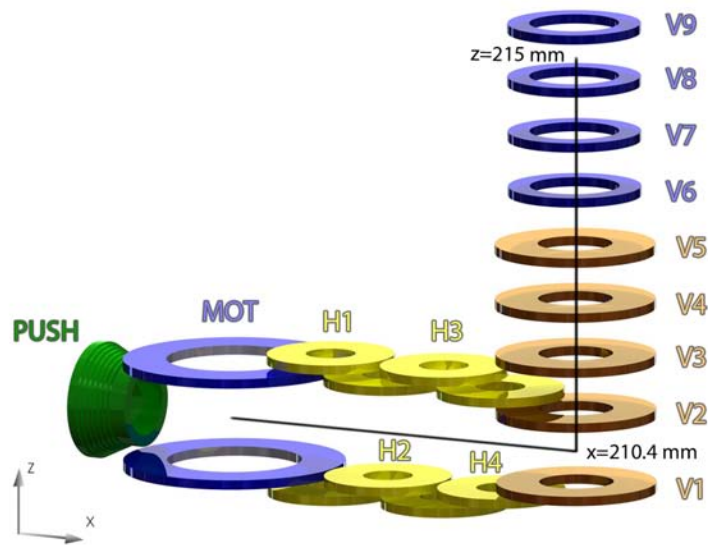


Figure 3.3.: A sketch of the transport scheme. The horizontal transport consists of the PUSH coil (green), the MOT coil-pair (blue), the horizontal coil-pairs H1 to H4 (yellow) and finally the pair V1/V2 in the corner. The vertical transport consists of the normal conducting coils V1 to V5 (orange) and the superconducting transport coils V6 to V9 (blue).

3.3. Magnetic transport

Fig.(3.3) shows a sketch of the coil-setup used for the magnetic transport. The magnetic trap is formed by the MOT-coils, the PUSH coil is used to push the atoms into the horizontal transport path which consists of the quadrupole coil pairs H1, H2, H3, H4 and finally V1/V2. The vertical transport consists of 5 normal conducting coils V1, V2, V3, V4, V5 and 4 super conducting coils V6, V7, V8 and V9 inside the cryostat. In this section, I describe the principles and calculations that lead to the used coil-currents according to [27]. In a first step, we calculated current over position curves for each of the coils/coil-pairs with *Mathematica*² described in Section 3.3.1, after that the current curves where imported into *Matlab*³ where current over time curves are created which can then be used as signal for the current supplies, shown in Section 3.3.2. Details about the current supplies are given in Section 4.4.

3.3.1. Current calculations

After loading the atoms into the magnetic trap, we need to move the trap position and respectively the magnetic field minimum in the desired transport direction. While

²Wolfram Mathematica 7

³MathWorks Matlab v7.9.0

doing this it is important that the atoms always see roughly the same trap potential and field gradient, a changing trap potential would heat the atoms or let them escape in the worst case. There are three crucial parameters which we need to take care of: First, the magnetic field has to be zero at the trap position as explained in Section 3.2. Second, the gradient in the vertical z-direction needs to be strong enough to compensate gravitation. The Zeeman-force in z-direction on ^{87}Rb atoms in the trap is calculated by Eq.(3.2).

$$F = \mu_B \frac{dB_z}{dz} \quad (3.2)$$

If we make the (hypothetic) assumption that the gravitation $F_g = mg$ (m is the mass of one rubidium atom) results also from a magnetic field gradient we can calculate a "gravitational magnetic gradient" $\left(\frac{dB_z}{dz}\right)_g$ of 0.153 T m^{-1} following Eq.(3.3).

$$F_g = mg = \mu_B \left(\frac{dB_z}{dz}\right)_g \Rightarrow \left(\frac{dB_z}{dz}\right)_g = \frac{mg}{\mu_B} \quad (3.3)$$

Consequently, the real magnetic gradient $\frac{dB_z}{dz}$ has to be big compared to 0.153 T m^{-1} to compensate gravitation. We chose a gradient of $\frac{dB_z}{dz} = 1.3 \text{ T m}^{-1}$ which meets this condition. Fig.(3.4) shows the influence of gravitation on the shape of the magnetic trap. While this influence on the quadrupole is neglectable for our case in the magnetic transport, gravitation could be an issue for a harmonic QulC-trap which is discussed in Section (3.4.1).

As third condition, the *aspect-ratio* A , defined in Eq.(3.4), needs to be stable throughout all phases of the transport.

$$A = \frac{dB_x/dx}{dB_y/dy} \quad (3.4)$$

For the considerations and calculations for the magnetic transport we split the transport line into the horizontal part and the vertical part. The reason for this distinction is that we have to consider different cases of the magnetic trap behavior depending on the direction the trap is moving. This is explained in detail in the following.

The horizontal transport

Starting point for the horizontal transport is the quadrupole trap in the center of the MOT chamber. After the molasses phase we trap the atoms in a quadrupole trap produced by the MOT coils, and ramp the trap gradient up to $dB_z/dz = 13 \cdot 10^{-2} \text{ T m}^{-1}$ (details about the ramp times are given in section 4.3). In a quadrupole trap in anti-Helmholtz-configuration the ratio $dB_z/dz : dB_x/dx = dB_z/dz : dB_y/dy$ is $2 : 1$ and consequently the aspect ratio $A = 1$. As we want to move the trap in x direction, we need to find a way to move the trap while keeping these parameters constant or changing them to values that are held constant. Simulations using

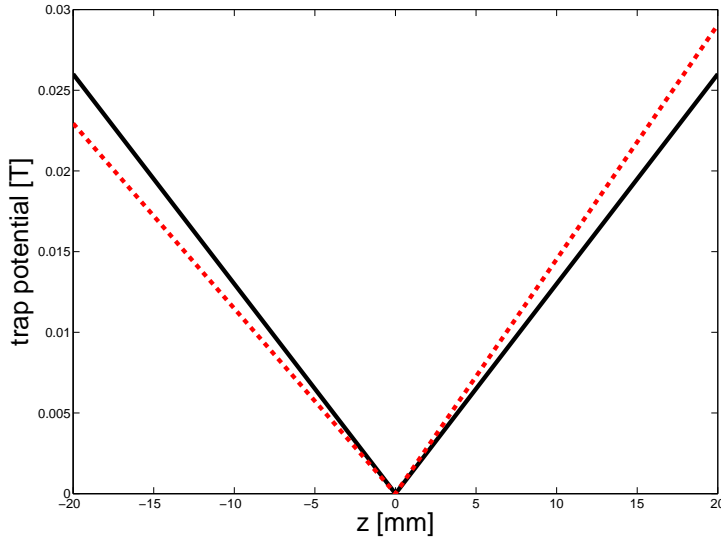


Figure 3.4.: The magnetic quadrupole trap without (black, solid line) and with (red, dashed line) the influence of gravitation. The trap is slightly tilted by gravitation but the tilt is small enough to be neglected.

Biot-Savart for each coil and super-positioning the resulting fields show that we need 3 pairs of quadrupole coils simultaneous to form a magnetic field which can keep A constant for every x position [27]. However, if we would keep $A = 1$ we would need bipolar currents in the transport quadrupole coils. We can avoid this by choosing $A = 1.715$ as constant value which is possible to realize by using only positive currents. This means that A has to be changed smoothly from 1 to 1.715 in the starting phase of the transport. This starting phase is done by the push-coil, the MOT coils and the first transport coil-pair H1. The behavior of the aspect-ratio over the x -position is shown in Fig.(3.5). For the vertical transport it is unavoidable to drive the transport coils with positive and negative currents, so we want to switch back to $A = 1$ at the end of the horizontal transport. In fact, the end of the horizontal transport can be seen as a loading procedure into another quadrupole trap formed by the last quadrupole-coil pair V1/V2.

In the part of the transport where A is kept constant, the currents for the coil-pairs are calculated using the conditions

- $B_z(x, 0, 0) = 0$
- $\frac{dB_z(x, 0, 0)}{dz} = 13 \cdot 10^{-2} \text{ T m}^{-1}$
- $A = 1.715$

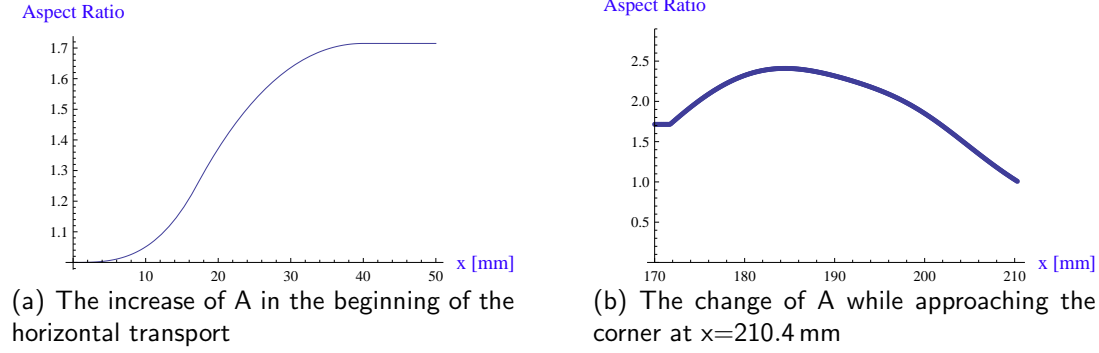


Figure 3.5.: The behavior of the aspect-ratio A over the horizontal transport line. In the region not shown A stays constant at 1.715

The gradients in the horizontal directions are then $dB_x/dx = 4.78 \cdot 10^{-2} \text{ T m}^{-1}$ and $dB_y/dy = 2.7 \cdot 10^{-2} \text{ T m}^{-1}$. The maximum horizontal transport distance is 210.4 mm. Figure 3.6 shows the resulting currents for all coil-pairs.

The vertical transport

After holding the atoms in the quadrupole trap of V1/V2 for 20 ms, we want to move them up in the center of the vertical transport coils as shown in Fig.(3.3). The vertical part consists of 5 normal conducting coils (V1-V5) and 4 super conducting coils (V6-V9) inside the cryostat. For moving the trap center through a coil it is clear that we need to change the polarity of the coil-currents. We use self made H bridges, which are simple transistor circuits that allow current from a power supply to be applied across a coil in either direction, to change the polarity of the current for the normal conducting coils. More details about the coil electronics can be found in [27] and [19]. For the superconducting coils we use two different power supplies for one coil.

Since the trap center is now always in the center of the coils the calculation is much simpler and can be done analytically (for the horizontal part the gradient could only be calculated by the differential quotient). Therefore the used conditions for the vertical currents are

- $B_z(x_{final}, 0, z) = 0$
- $\frac{dB_z(x_{final}, 0, z)}{dz} = 13 \cdot 10^{-2} \text{ T m}^{-1}$
- $\frac{d^2 B_z(x_{final}, 0, z)}{dz^2} = 0$
- $\sum_i^n (I_n \cdot N_n) = 0$

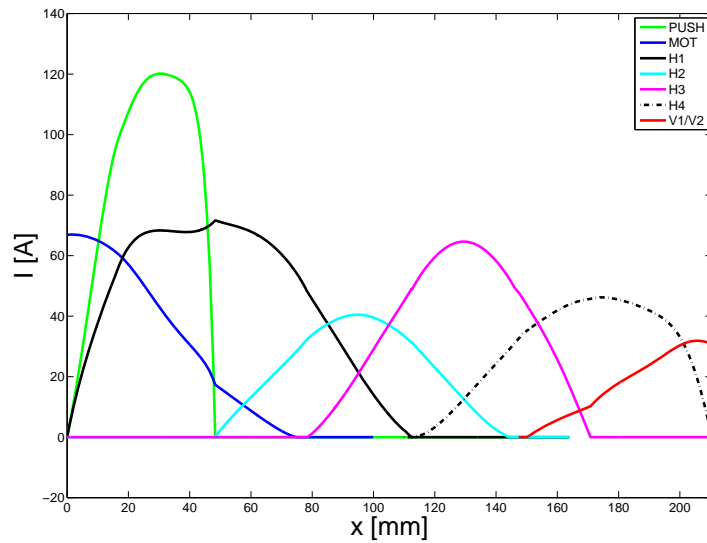


Figure 3.6.: The calculated currents for the horizontal transport coil-pairs. One can see the strong current needed in the PUSH-coil to get the transport started.

For the vertical part we measure the currents in integrated currents since the current is a factor 100 lower in the super conducting coils which compensate this with a higher number of windings (The super conducting coils have 3000 windings compared to 40 for the normal conducting ones). This leads to the last condition that means that the sum over all used coil-currents times the number of windings of the used coil should always be zero. The calculation showed to be very stable with this condition, although it is only met in the positions where 4 coils form the magnetic trap. Fig.(3.7) shows the ampere-turns resulting from the calculation. The first current needs to be stronger compared to the following coils because in the beginning of the vertical transport we have a distance between V1 and V2 of 40 mm compared to a distance of 30 mm between every other two vertical coils (see Fig.(3.3)). The ideal calculated curves have been modified afterwards to consider geometrical inaccuracies that occurred in manufacturing and building the transport.

3.3.2. Time calculations

In the last section I showed how we calculate the current over position curves needed for a smooth transport of ^{87}Rb atoms. The signal sent to the current supplies needs of course to be a current over time ($I(t)$) signal which is created by the use of changeable variables that give us the opportunity to control the timing of the transport. To get to a $I(t)$ curve we first calculate a $x(t)$ and $z(t)$ curve so we can assign a time to each position and therefore, with the use of the previously calculated $I(x)$ and $I(z)$ curves, a current to each time value. This is done again separately for the horizontal and the

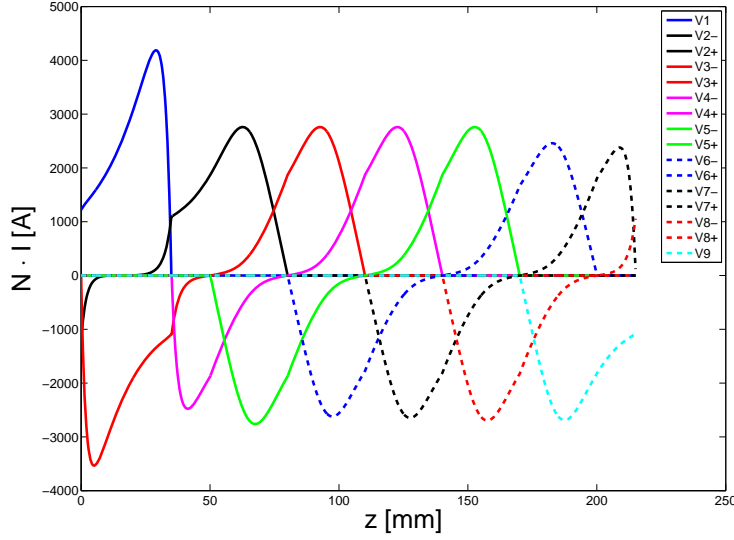


Figure 3.7.: The calculated integrated currents for the vertical transport coil-pairs. In the beginning the currents need to be higher compared to the rest of the transport because we must compensate for a higher distance of V1 and V2 (40 mm) compared to the other ones (30 mm).

vertical part. The main reason for this is that in the vertical part we have to consider that the superconducting coils, due to their high conductivity (about 540 mH), can't be ramped arbitrary fast. Our current sources are supplied by a voltage of $V_S = 15\text{ V}$. Therefore for driving a certain current curve the current source can't output a voltage higher than V_S . The fastest way to ramp the current up would be an instant rise from 0V to 15V. Solving the differential equation (Eq.(3.5)) for a circuit with a resistance R and an inductivity L in series driven by a constant voltage V_S leads to an exponential behavior of the current (Eq.(3.6)).

$$V_S = R \cdot I(t) - L \frac{dI(t)}{dt} \quad (3.5)$$

$$I(t) = \frac{V_S}{R} \cdot \left(1 - e^{-\frac{tR}{L}}\right) \quad (3.6)$$

The theoretically fastest possible ramp is shown in Fig.(3.8). The calculation shows that it is impossible to ramp the current in less than 36.6 ms to 1 A. Since our current source is not ideal and needs time to ramp up the voltage to maximum, the real limit is higher at about 50 ms.

Therefore we need to control the transport velocity in the vertical part. This section describes the used parameters and principles of the calculations for $x(t)$ and $z(t)$ and further $I(t)$ curves.

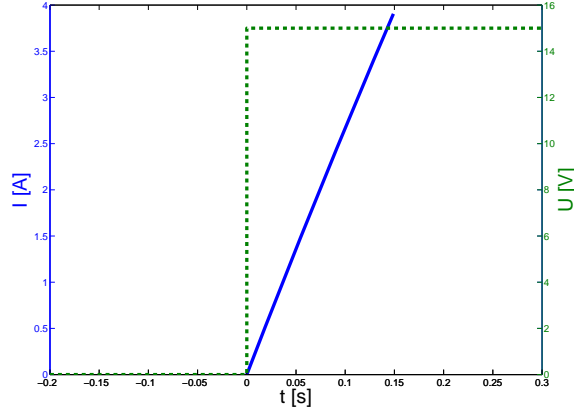


Figure 3.8.: The calculated current ramp when switching 15 V on the coil circuit. When the voltage (green dashed line) is switched on the current (blue solid line) rises following Eq.(3.6). This is an ideal calculation for a superconducting coil with a resistance $R=0.4\Omega$ of the normal conducting wires and an inductivity of $L=540$ mH.

The horizontal part

For the horizontal line we use a system of always varying the transport velocity. This means that we accelerate the atoms out of the magnetic quadrupole trap to a certain maximum velocity and decelerate them again instantly after reaching the maximum to $v = 0$ at the desired transport position. An actual graph of velocity, acceleration and position in dependence of time is shown in Fig.(3.9). The parameters we control are the final position atoms are transported to ($x_{final} \in \{0, 210.4\}$ mm), the time T when x_{final} is reached and the time T_{max} when the maximum velocity (which we *can not* directly control) is reached. For the calculation of a corresponding $x(t)$ curve we split the transport path in two areas, $t_1 < T_{max}$ and $t_2 \geq T_{max}$. For each of these areas we use a quadratic polynomial as ansatz for the acceleration.

$$a_1(t_1) = 3C_{11} \cdot t_1^2 + 2C_{12} \cdot t_1 \quad a_2(t_2) = 3C_{21} \cdot t_2^2 + 2C_{22} \cdot t_2 \quad (3.7)$$

C_{11} , C_{12} , C_{21} and C_{22} are the constants we want to define. Integration of equation 3.7 leads for the corresponding velocity and position to

$$v_1(t_1) = C_{11} \cdot t_1^3 + C_{12} \cdot t_1 + v_{10} \quad (3.8a)$$

$$x_1(t_1) = \frac{1}{4}C_{11} \cdot t_1^4 + \frac{1}{3}C_{12} \cdot t_1 + \frac{1}{2}v_{10} + x_{10} \quad (3.8b)$$

$$v_2(t_2) = C_{21} \cdot t_2^3 + C_{22} \cdot t_2 + v_{20} \quad (3.8c)$$

$$x_2(t_2) = \frac{1}{4}C_{21} \cdot t_2^4 + \frac{1}{3}C_{22} \cdot t_2 + \frac{1}{2}v_{20} + x_{20} \quad (3.8d)$$

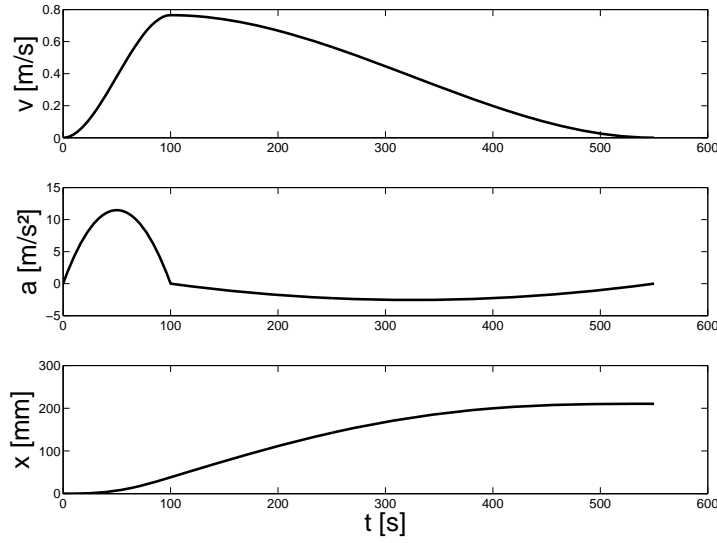


Figure 3.9.: The velocity, acceleration and position curves in dependence of the transport time for the horizontal transport. This is an example with the parameters $T = 550\text{ms}$, $T_{max} = 100\text{ms}$ and $x_{final} = 210.4\text{ mm}$.

The task is now to find the parameters C_{11} , C_{12} , C_{21} , C_{22} , v_{10} , v_{20} , x_{10} and x_{20} for the parameters T , x_{final} and T_{max} . This is done by setting up a system of equations following the conditions

- $x_1(0) = 0$, $x_1(T_{max}) = x_2(T_{max})$, $x_2(T) = x_{final}$
- $v_1(0) = 0$, $v_1(T_{max}) = v_2(T_{max})$, $v_2(T) = 0$
- $a_1(0) = 0$, $a_1(T_{max}) = a_2(T_{max}) = 0$, $a_2(T) = 0$

Solving this system leads to a curve $x(t)$ depending on T , T_{max} and x_{final} as shown in Fig.(3.9). With this we can get from the previously calculated $I(x)$ curve to a $I(t)$ curve which is converted to ADwin-format and sent to the ADwin system (refer to section 4.5 for details about the ADwin system).

For testing the transport we need to transport the atoms to a certain point of the transport path and go then back to the MOT chamber for imaging and measuring the atom cloud. Therefore, if we do not want to transport one way into the cryo chamber, we have the possibility to chose a bidirectional transport by reversing the calculated $x(t)$ curve and add it to first curve after reaching x_{final} . We don't need this if we want to transport up into the cryostat, of course x_{final} must then be at the maximum value of 210.4 mm to get in the right position for the vertical transport.

The vertical part

As stated above, we need to control the maximum velocity for the vertical transport path. Therefore we use a different calculation theme for the needed $z(t)$ curves. Here the parameters we chose are the maximum velocity v_0 , the maximum acceleration a_{max} and the final transport position z_{final} (this has to be set to the maximum value of 215 mm if we want to image in the cryostat). We presume the rise of the acceleration to a_{max} as a third degree polynomial (Eq.(3.9)) where we reach the velocity v_{max} . After that we use the same polynomial function to lower the acceleration to zero and reach v_0 . Therefore $v_{max} = \frac{v_0}{2}$. The time when maximum acceleration is reached (t_{max}) depends on a_{max} and v_0 .

$$a(t) = A \cdot t^3 + B \cdot t^2 \quad (3.9)$$

Integration of the acceleration leads to

$$v(t) = \frac{A}{4} \cdot t^4 + \frac{B}{3} \cdot t^3 + C \quad (3.10a)$$

$$z(t) = \frac{A}{20} \cdot t^5 + \frac{B}{12} \cdot t^4 + C \cdot t + D \quad (3.10b)$$

We use the conditions $v(0) = C = 0$, $z(0) = D = 0$, $a(t_{max}) = a_{max}$, $\frac{d}{dt}a(t_{max}) = 0$ and $v(t_{max}) = v_{max}$, where t_{max} is the time when a_{max} and v_{max} is reached. This leads to the solution for A , B and t_{max} :

$$A = -\frac{a_{max}^4}{4v_{max}^3}; \quad B = \frac{3a_{max}^3}{4v_{max}^2}; \quad t_{max} = \frac{2v_{max}}{a_{max}} \quad (3.11)$$

We have to consider the possibility that z_{final} is so small that we don't reach the velocity v_0 with the given acceleration a_{max} . In this case $z_{final} \leq z_{crit} = \frac{8v_{max}^2}{a_{max}} = \frac{2v_0}{a_{max}}$ and the above described calculation is not valid anymore. Then we have no area of constant velocity, instead we split the transport path into 4 parts with the duration $t_{max} = \frac{2v_{max}}{a_{max}}$. This way we accelerate to a new value $v'_0 < v_0$ with the maximum acceleration $a'_{max} < a_{max}$ to still have a pattern of smooth acceleration and deceleration shown in Fig.(3.11). With the currently used values $a_{max} = 4 \text{ m/s}^2$ and $v_0 = 0.15 \text{ m/s}$, this only matters when z_{final} is lower than 11.25 mm. Most of the time we don't need such a short transport distance so the previously described scheme is used. However, we have implemented the necessary modifications to be able to transport such a short vertical distance.

3.4. The Quadrupole Ioffe trap

Once transported to z_{final} following the mechanisms described in the previous chapter we have the atoms trapped in a quadrupole trap inside the cryostat. The final step

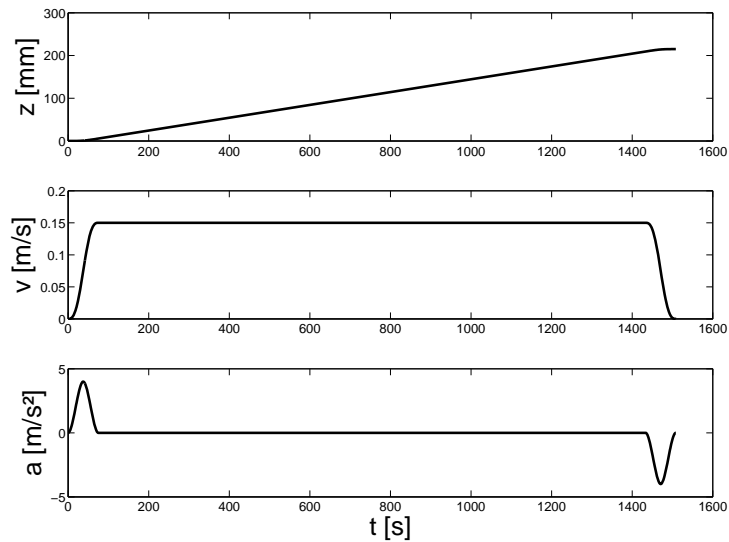


Figure 3.10.: Transport parameters for the vertical transport, $z(t)$, $v(t)$ and $a(t)$. The chosen parameters are $a_{max} = 4 \text{ m/s}^2$, $v_0 = 0.15 \text{ m/s}$ and $z_{final} = 215 \text{ mm}$. This is the transport into the quadrupole trap in the cryostat.

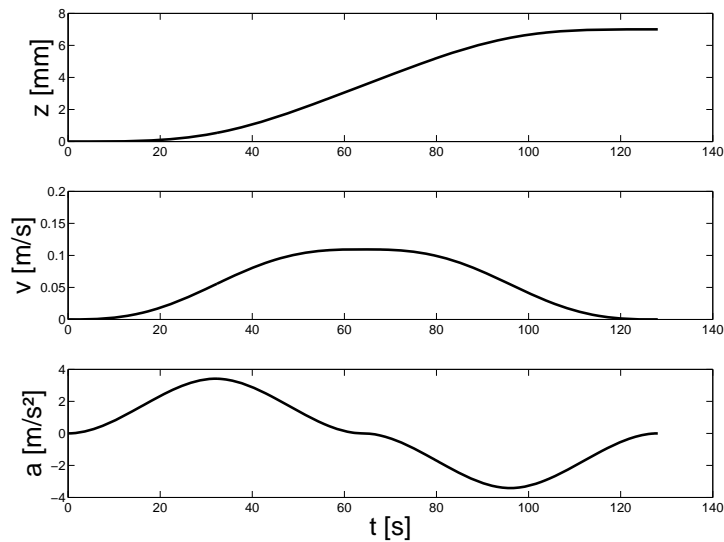


Figure 3.11.: Vertical transport parameters for the case $z_{final} \leq z_{crit}$. The chosen parameters are $a_{max} = 4 \text{ m/s}^2$, $v_0 = 0.15 \text{ m/s}$ and $z_{final} = 7 \text{ mm}$. The graph shows that a_{max} and v_0 are not reached anymore.

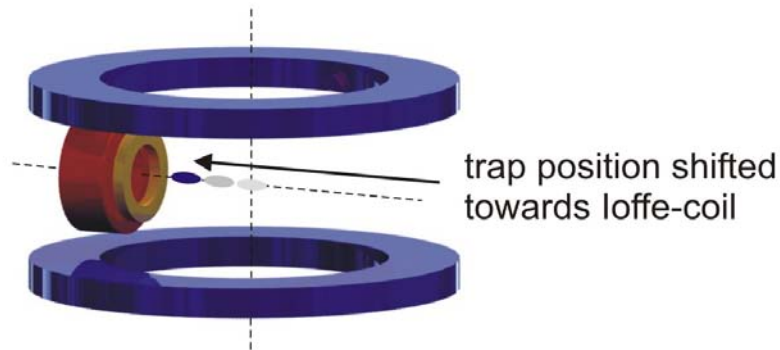


Figure 3.12.: Coil setup for the quadrupole-Ioffe-trap.

to cool atoms down to a BEC is evaporative cooling. In the evaporative cooling procedure the height of the magnetic trap potential is gradually reduced, allowing the fastest and hottest atoms to escape. This lowers the number of atoms as well as the temperature, since the escaping atoms carry away more than the average amount of energy [15]. In a linear trap potential one observes a loss of atoms when getting to very low temperatures. This is because atoms that sit in the trap minimum where $B = 0$ can flip their spin and therefore change to an untrapped state, which is called *Majorana losses* [35]. This makes reaching a BEC in a linear trap potential (of a quadrupole trap) impossible.

Therefore we need to change the trapping potential to a potential with a non-zero trap bottom. Our way to do this is with the quadrupole-Ioffe-trap configuration shown in Fig.(3.12) [13]. Additionally to the last two transport coils V8 and V9, we implement an Ioffe coil in orthogonal direction to the quadrupole coils. A simple simulation considering ideal coils with one current loop and neglecting the real dimensions shows a change of the trap potential with ramping up the current through the Ioffe coil. In Fig.(3.13) we calculated four different states of the trap, increasing the Ioffe current from top to bottom. The dashed line shows the quadrupole trap potential without considering the Ioffe current, the dotted line is the potential from the isolated Ioffe coil and the solid line is the combined trap potential. In case a) the Ioffe current is low and the potential in the trap center is still linear with $B = 0$ at the center. When we increase the current the Ioffe potential intersects the quadrupole potential in two points which leads to a the trap potential shown in b) with two minima. With further increasing the dotted Ioffe-field moves up and the trap minima move closer until they unite to a harmonic potential at point c). After this we can raise the trap bottom with increasing the current further. d) shows finally the case of a harmonic trap with a trap bottom of about 25 G. A trap of this shape could be used for evaporative cooling and to prevent Majorana losses. First results of atoms in the Ioffe trap are shown in Section 5.2.

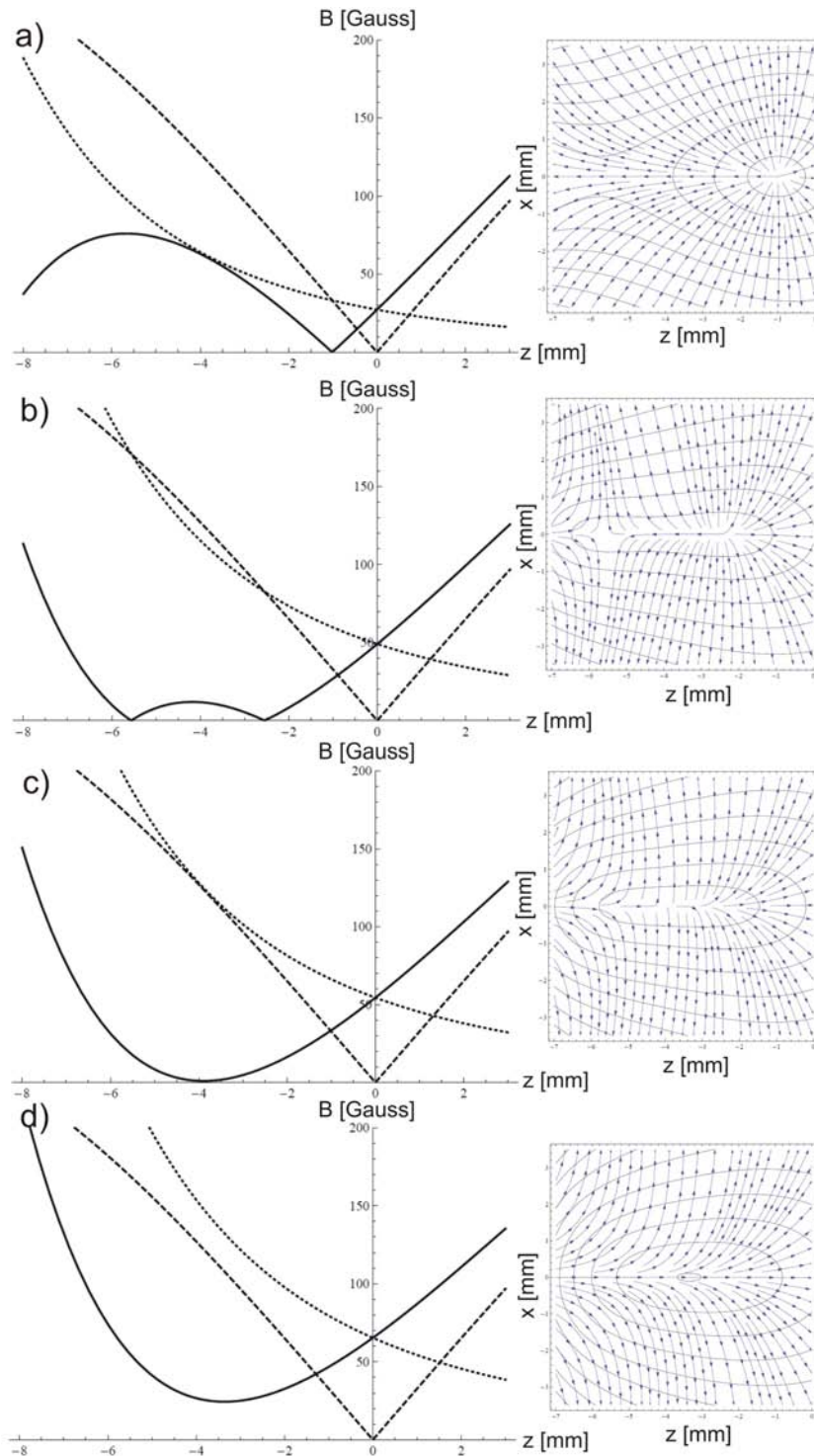


Figure 3.13.: The change of the magnetic trap potential along the coil axis (longitudinal) with increasing the Ioffe current. The dashed line shows the quadrupole trap of V_8 and V_9 , the dotted line the field of the Ioffe-coil and the solid line the resulting trap shape. The inset on the right gives a two dimensional plot for the directions normal to the coil-axis (transversal). See text for further explanations. Taken from [19].

3.4.1. Influence of gravitation on the QulC-trap

It was shown in Section (3.3.1) that the influence of gravitation on the magnetic quadrupole trap is neglectable and the shape of the trap doesn't change significantly. Since we have a harmonic potential in the QulC trap we have to investigate again if and how the trap potential changes by gravitation. For a rough quantitative estimation of this effect, we look at a simple undisturbed harmonic trap potential given by Eq.(3.12a), with the trap frequency ω and the non-zero trap bottom $B_0 = B(z = 0)$ at the trap-center. The "gravitation gradient" derived in Section (3.3.1) multiplied with the position on the z-axis will be super-positioned with the harmonic potential resulting in the changed trap geometry $B'(z)$ (Eq.(3.12b)).

$$E(z) = \mu_B B(z) = \frac{1}{2} m \omega^2 z^2 + \mu_B B_0 \quad (3.12a)$$

$$E'(z) = \mu_B B'(z) = \frac{1}{2} m \omega^2 z^2 + \mu_B B_0 + \left(\frac{dB}{dz} \right)_g z \quad (3.12b)$$

For a numerical analysis we assume typical (ideal) values for our trap. We chose a trap bottom of 10^{-4} T (1 G), a trap frequency along the Ioffe-coil-axis (longitudinal) of $2\pi \times 20$ Hz and a transversal (normal to the Ioffe-coil-axis) trap frequency of $2\pi \times 500$ Hz. Fig.(3.14) shows a comparison between the longitudinal and the transversal trap geometries. The solid blue and black curves are the undisturbed harmonic traps for the longitudinal and transversal directions. As illustrated in Fig.(3.12) the gravitational z-axis lies in transversal direction (black curve in Fig.(3.14)). When applying gravitation (red dotted curve) the trap potential changes hardly and the potentials overlap. Fig.(3.15) shows a zoomed view of Fig.(3.14) where we can observe the change in potential which is neglectable. However, if we would consider having a trap frequency similar to the longitudinal direction or having the whole trap tilted by 90° in a way that the Ioffe-coil-axis would be in z-direction, the change to the trap potential would be significant. This can be seen by comparing the longitudinal trap potential (blue, solid curve) with the shifted potential by gravity (blue, dashed curve) in Fig.(3.14). In this case we would see a major change in the potential, the overall potential would be shifted 0.622 mm compared to the magnetic trap. Therefore, the atoms would not be trapped in the center of the magnetic trap potential which would inhibit effective evaporative cooling.

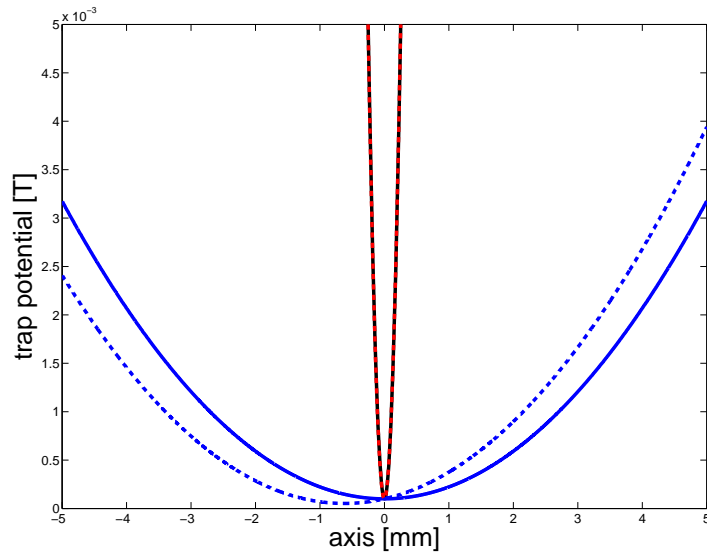


Figure 3.14.: The Ioffe-trap-potential in longitudinal (solid blue line) and transversal (black line) direction. The influence of gravitation on the trap geometry is given by the red, dashed line. For demonstration the hypothetical change of the longitudinal trap potential by gravitation is shown (dashed blue line), which would result in a significant shift of the trap position (0.622 mm).

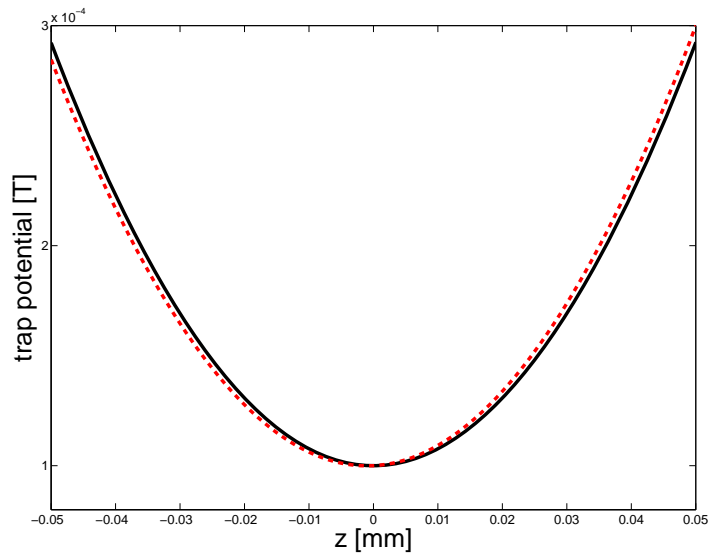


Figure 3.15.: More precise view of the change of the QulC-trap potential by gravitation. The trap position is shifted by 1 μm in the simulation which can be neglected.

4. Experimental realization

4.1. Vacuum Setup and the Cryostat

4.1.1. General Setup

The lower part of the experiment is shown in Fig.(4.1). The MOT chamber was manufactured in the workshop of the Atominstitut. It is made out of 316 L steel and has CF40 laser windows mounted on the three axis of the MOT, on one additional horizontal imaging axis and on a small CF10 window in the center of the push coil (green in Fig.(4.1)) for direct observation in direction of the transport axis. By pumping the MOT chamber with a 50l/s ion pump, we reach a minimal pressure of 1×10^{-10} mbar and a pressure around 6.5×10^{-9} mbar during operation. Midway of the horizontal transport line, we have a VAT¹ vacuum valve to separate the lower chamber from the vertical transport way into the cryostat. The lower part of the vertical transport is additionally connected to a smaller 20l/s ion pump, to sustain the vacuum during the transport. For evaporating ⁸⁷Rb atoms into the chamber by thermic emission, we use an alkali metal evaporation dispenser from the company SAES [17] connected to the chamber, which is operated constantly at about 7 W when the transport is running.

The cryostat is a closed cycle cryo-cooler² (Fig.(4.2a)) which uses a pneumatically driven Gifford-McMahon cooling cycle . It operates with a closed-loop Helium cycle with two stages [11]. The moving parts of the cryostat are mechanically decoupled from the cooling finger via a helium belly to minimize vibrations on the experiment. The vibrations on the experimental stage were measured to be below 106 nm [4]. A radiation shield made from high purity aluminium shown in Fig.(4.3) is connected to the first stage which gets a measured temperature of about 55 K. It is made from two parts to allow easy access to the coil-cage (Fig.(4.22)). In the lower part we can mount 4 images for optical access, at the moment only two windows are built in. The base of the coil-cage is directly mounted on the cooling finger which is cooled to 4.2 K in the ideal case. With all coils and charcoal (see Section 4.4.4 and Fig.(4.26)) built in we reach a base temperature of about 5 K.

The cryo-chamber (Fig.(4.2b)) is connected via a CF10 flange to the lower part of the

¹VAT vacuum valves - www.vatvalve.com

²Advanced Research Systems (ARS) CS204*F-DMX-20B - www.arscryo.com

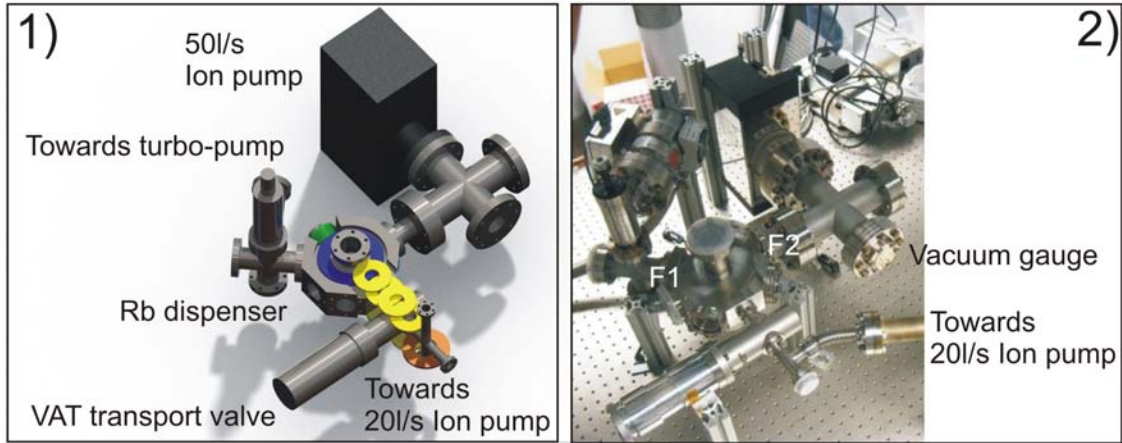


Figure 4.1.: Sketch (1) and photograph (2) of the MOT chamber and lower transport. (Taken from [19])

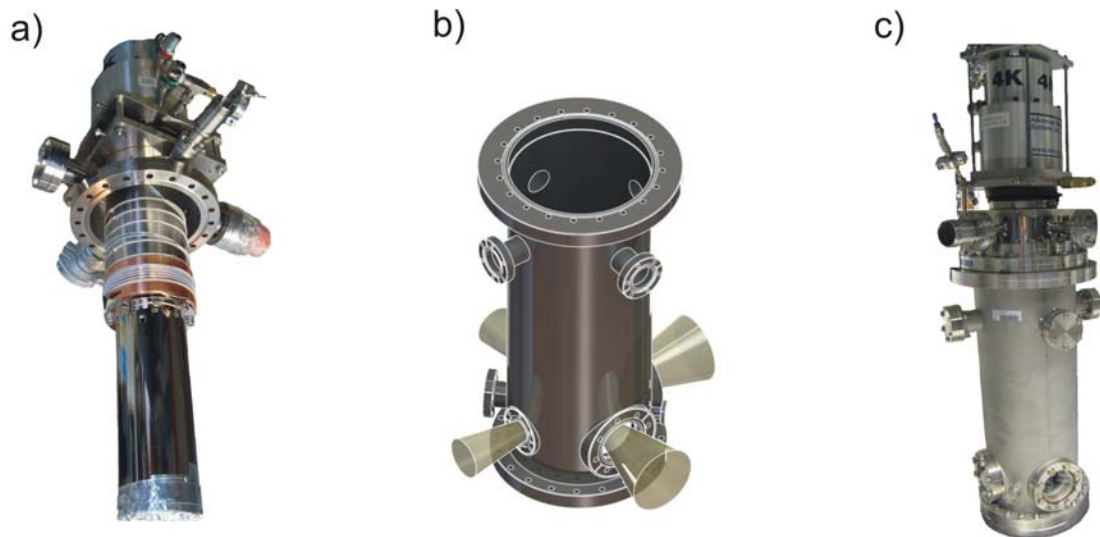


Figure 4.2.: Cryostat and cryo-finger (a), cryo-chamber (b) and the connected setup (c). (Taken from [19])

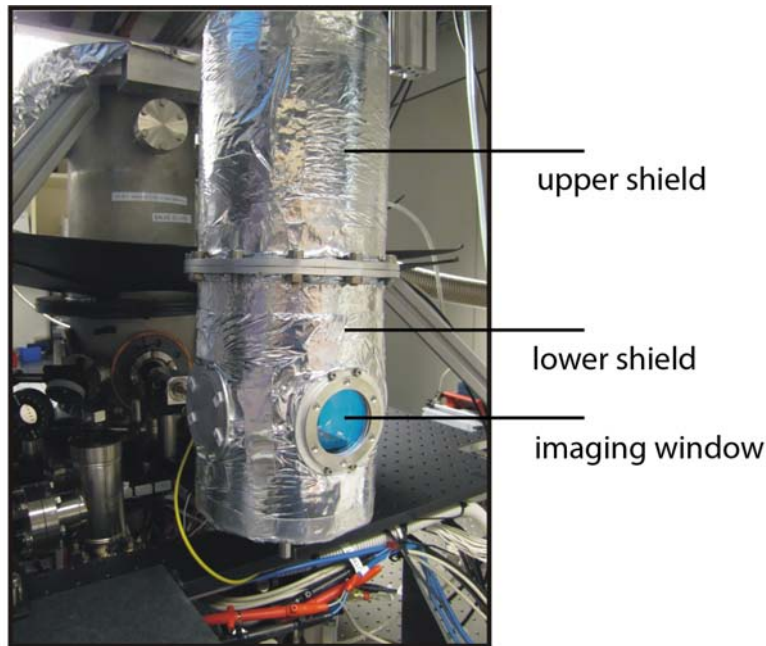


Figure 4.3.: Photograph of the thermal shield consisting of two parts connected to the first cooling stage of the cryostat.

transport (small vertical tube in Fig.(4.1a). It has for each optical axis in height of the final experiment position between V8 and V9 a CF40 and a CF63 laser window, and additionally on a 45° axis a CF16 and a CF40 flange where it would also be possible to mount windows. On the upper part of the chamber 4 CF40 flanges are mounted. On one a TMP³ and an oilfree rotary vane pump⁴ are connected who allow us to pump the chamber to a vacuum of 10^{-5} mbar at room temperature. With the cryo cooled we reach 10^{-10} mbar in the optimal case. We measure this with a vacuum gage⁵ mounted on a second CF40 flange. The other two flanges are not used and sealed. On the upper end of the chamber we connect the cryostat to the chamber by sealing a CF200 flange. Since we want to be able to change elements on the experimental stage with the least effort, the cryo finger was mounted on a construction with a cable pull that allows us to move the whole cryostat in and out of the chamber. The system is than opened (closed) only by opening(closing) the CF200 flange which makes changing some details on the experiment quite easy and comfortable. We are able to pump and cool down to 5 K on the experimental stage in about 7 h and have the experiment running within a day. This is a strong advantage compared to cold atom experiments on room temperature, which have to be pumped and baked for weeks to reach the necessary vacuum. The warm up process takes

³Pfeiffer VACUUM TMU 071P

⁴Pfeiffer VACUUM MVP 055-3

⁵Pfeiffer VACUUM Compact FullRange Gauge PKR 251

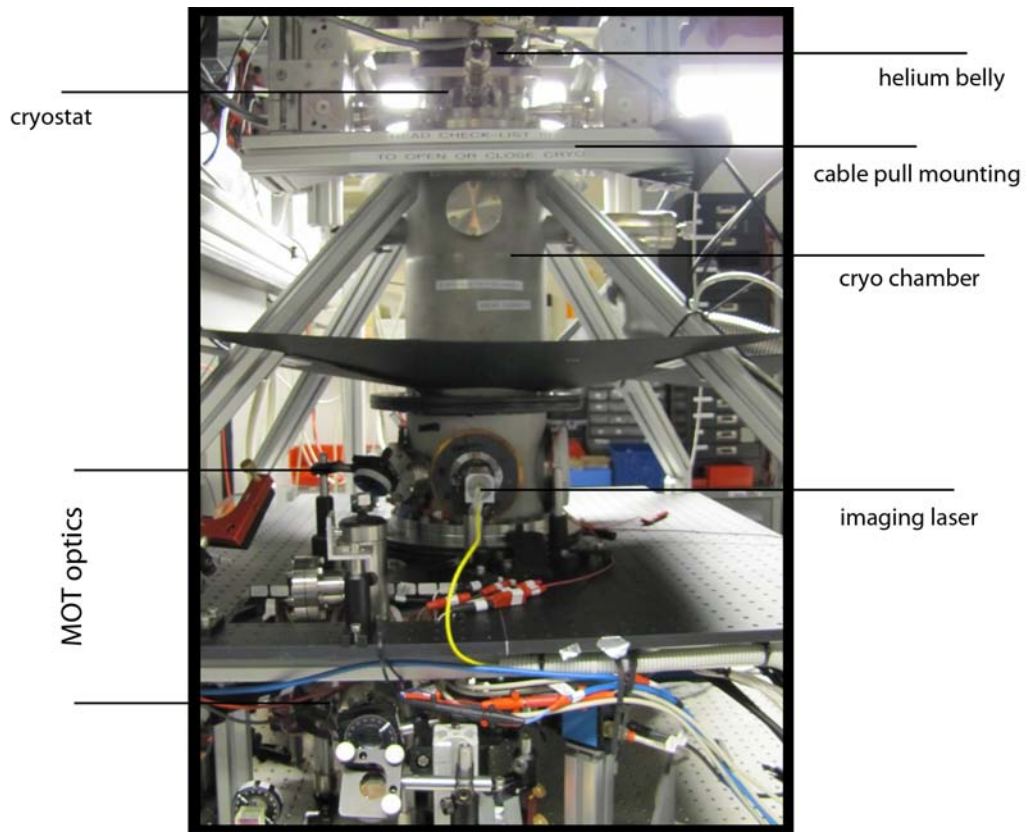


Figure 4.4.: Photograph of the vacuum-chamber, cryostat and parts of the MOT optics.

normally about 14 h, but we are able to accelerate this by pumping helium gas into the chamber to as low as 5 h. Fig.(4.4) shows our apparatus in closed state.

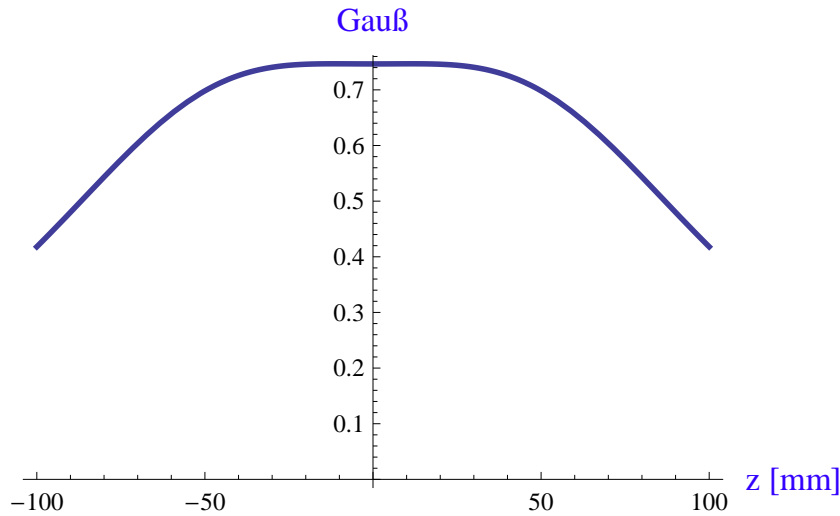


Figure 4.5.: Field produced by a MOT compensation coil-pair in perfect Helmholtz-configuration $r_H = 1$.

4.1.2. Compensation Coils

For having a well defined magnetic field which can be controlled with our trap coils we need to compensate the earth magnetic field of about 0.7 G to get a clean trap. We can do this with three additional compensation coil pairs ideally in Helmholtz configuration for all three spacial directions. For the MOT chamber this was realised with two quadratic coil pairs with a sidelength ($2R$) of 180 mm and a distance (d) of 90 mm, which meets exactly the ideal Helmholtz ratio of $r_H = \frac{R}{d} = 1$. The absolute value of the resulting magnetic field in the MOT chamber is shown in Fig.(4.5). This configuration leads to a constant field in the trap center. For the vertical axis circular coils of the same size (a diameter of 180 mm in a distance of 90 mm) were used.

Considering the compensation fields in the cryostat, the ideal Helmholtz-configuration was possible to realise in the vertical direction by mounting the coils directly on the cryo chamber (see Fig.(4.2b)) with a diameter of 300 mm and a distance of 150 mm. A mounting made of 4 PVC parts which could be attached to the cryo chamber was manufactured in the mechanical workshop (Fig.(4.9b)). In the horizontal directions it was impossible to meet Helmholtz-configuration because there was simply no place to mount the coils with the right dimensions. So we investigated three different options for mounting the coils (Fig.(4.6)):

1. Mounting circular coils directly on the CF63/CF40 flanges of the cryo-chamber. This would be the most practicable option, but with the dimensions $2R = 116\text{mm}$ and $d = 205\text{mm}$ which leads to $r_H = 0.3$ far away from ideal and the resulting field would not be constant in the trap region.
2. Mounting quadratic coils on the laser-breadboard which holds MOT- and imag-

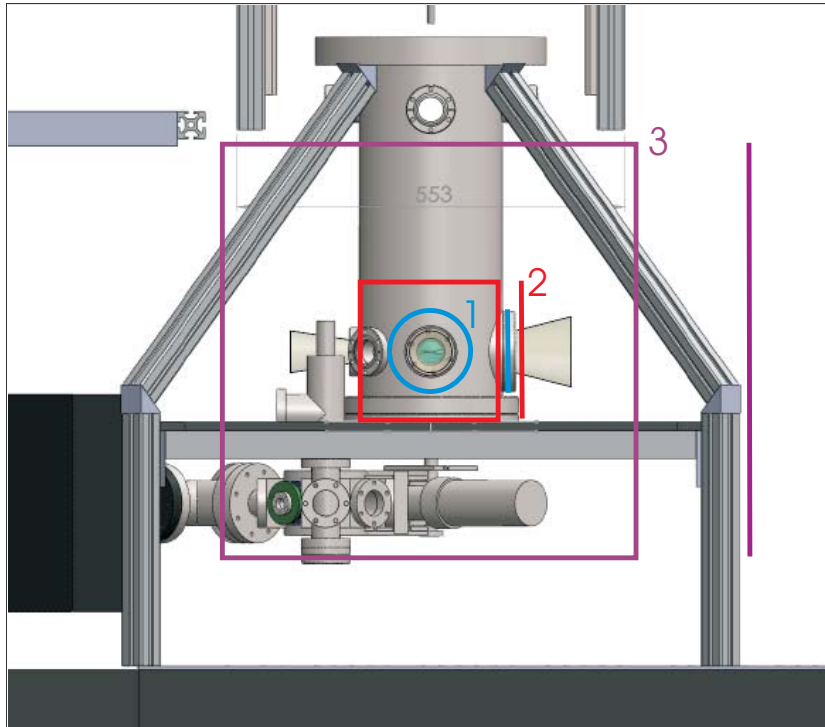


Figure 4.6.: Three alternative solutions for the horizontal compensation coils. 1/blue: The coils are wound on mountings attached to the vacuum flanges, 2/red: Quadratic coils attached to the breadboard, 3/purple: Quadratic coils attached to the edges of the breadboard.

ing optics. Here a slightly better Helmholtz-like configuration would be possible ($2R = 170\text{mm}$ and $d = 280\text{mm} \rightarrow r_H = 0.304$), at the expense of place on the breadboard.

3. Mounting huge quadratic coils around the whole experiment. This would lead with $2R = 670\text{mm}$ and $d = 1000\text{mm}$ and $r_H = 0.335$ to the best option regarding the field but would be a big construction which may be disadvantageous for further experimental developments and installations.

The problem with a design that results in $r_H \neq 1$ is that the field gradient $\frac{dB}{dz}$ is not zero at the trap position. This results in an additional Zeeman shift and a change in the desired trap potential. Fig.(4.7) shows the calculated magnetic field change for all coil options near the trap center ($z = \pm 1\text{ mm}$ which we considered to be the maximum size of a condensed atomcloud). To see if this change in potential is a problem for our experiment, we considered quantitatively two consequences. First the absolute shift of the magnetic field ΔB which results in a shift of the Zeeman splitting ΔE_Z following Eq.(4.1).

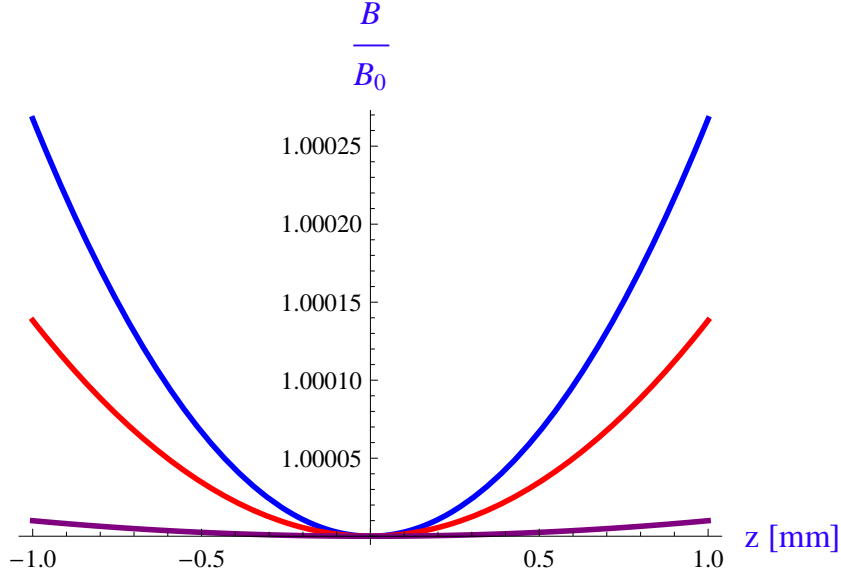


Figure 4.7.: Comparison of the relative field change $\frac{B}{B_0}$ for the coil options 1 (blue), 2 (red) and 3 (purple).

$$\Delta E_Z = g_F m_F \mu_B \Delta B \quad \Rightarrow \quad \Delta E_Z = \mu_B \Delta B$$

$$\text{with } g_F(^{87}\text{Rb}) = \frac{1}{2} \text{ and } m_F(\text{trap}) = 2 \quad (4.1)$$

Second, the energy shift produces a force on the atoms in a gradient field which leads to an additional velocity on the rubidium atoms and could therefore heat up the atomcloud or the BEC (Eq.(4.2)). m depicts the mass of one ^{87}Rb atom.

$$F = \mu_B \nabla B = m \frac{dv_B}{dt} \quad (4.2a)$$

$$v_B = \int \frac{1}{m} \mu_B \nabla B dt = v_0 + \underbrace{\frac{1}{m} \mu_B \nabla B t}_{\Delta v_B} \quad (4.2b)$$

We can compare this additional velocity Δv_B to the average thermal velocity of a BEC \bar{v}_T which can be approximated by the model for an ideal gas (Eq.(4.3)). For the typical condensation temperature of 1 μK for a trapped atomic gas the thermal

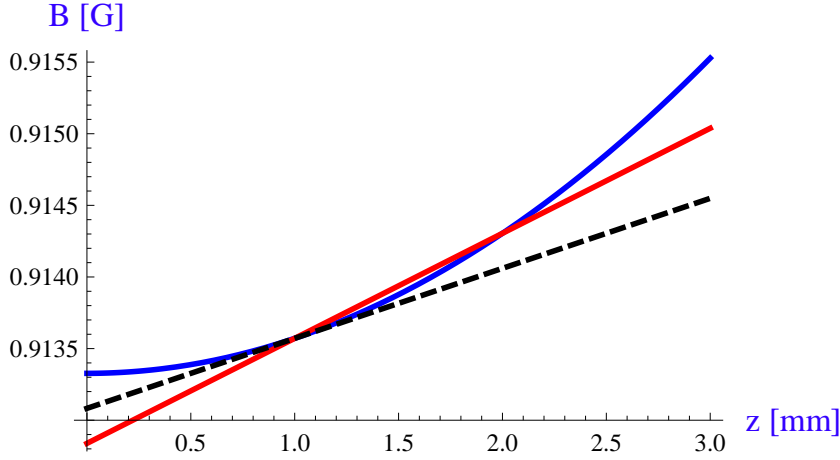


Figure 4.8.: To estimate the gradient $\frac{dB}{dz}$ at the position $z = 1$ mm (slope of the black, slashed line) we used the difference $B[z = 2] - B[z = 1]$, which is the slope of the solid red line. As the figure shows, this leads to an overestimation of the gradient.

velocity in this approximation gives $\overline{v_T} = 1.7 \times 10^{-2}$ m/s [15].

$$E_{kin} = \frac{m\overline{v_T}^2}{2} = \frac{3}{2}k_B T \quad (4.3a)$$

$$\overline{v_T} = \sqrt{\frac{3k_B T}{m}} \quad (4.3b)$$

Tab.(4.2) shows the simulated results for the three coil options. For calculating the gradient in Eq.(4.2) we used an overestimation explained in the caption of Fig.(4.8) to have some headroom. We need an value for the exposure time t for calculating Δv_B , we chose 20 ms as this is a usual value for a BEC experiment. As expected, mounting the coils directly on the vacuum flanges (Option 1) influences the experiment the most. The shift of the magnetic field is in the worst case $\Delta B = 2.15 \cdot 10^{-4}$ G which is still neglectable compared to a trap field of ≈ 1 G. The additional velocity for atoms in the trap cooled down to a BEC is only 0.244% of v_T and will therefore produce no additional heating.

Considering these results we decided that we can go with the most practicable option 1. Mountings out of PVC where manufactured by the workshop (see A.2 for technical drawings) and we used a copper wire with a diameter of 400 μm wind the coils on them. Fig.(4.9) shows the finished coil setup on the cryostat.

	Option 1	Option 2	Option 3
ΔB [μG]	215	78.3	1.68
ΔB [nK]	14.4	5.3	0.1
ΔE [Hz]	317,27	115,56	2,47
Δv_B [mm/s]	$4.14 \cdot 10^{-2}$	$1.51 \cdot 10^{-2}$	$3.23 \cdot 10^{-4}$
$\frac{\Delta v_B}{v_T}$ [%]	$2.44 \cdot 10^{-1}$	$8.88 \cdot 10^{-2}$	$1.90 \cdot 10^{-3}$

Table 4.1.: Simulation results for all three coil options. Option 1 has the strongest shifts, nevertheless they are small enough to be neglected (see text for further explanation).

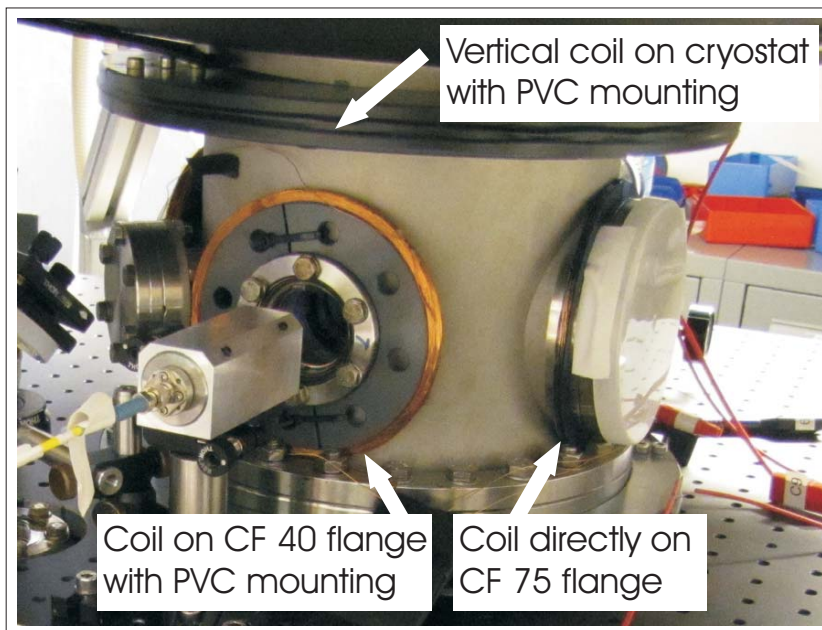


Figure 4.9.: Photograph of the PVC mountings and the coils attached to the cryostat and flanges in the final realized setup (Option 1).

Coilpair	Connectors	R [mm]	h [mm]	N	$R[\Omega]$	d [mm]	$B(I)$ [$\frac{G}{A}$]	I_{max} [A]
Horizontal 1	C1/C2	60	10	100	10.4	205	2.81	0.4
Horizontal 2	C4/C5	60	10	100	10.4	205	2.81	0.4
Vertical	C7/C8	150	3	50	13.4	190	2.47	0.4

Table 4.2.: Properties of the designed compensation coils. R is the inner radius of each of the coils, h the height of the coil itself, N the number of windings of each coil, R the resistance and d the distance between the coils. The current needed to produce a magnetic field of 0.7 G in the center to compensate the earth magnetic field is I_g . For the used AWG 26 wire the maximum steady current is $I_{max} = 0.4$ A [39].

4.2. Lasers and Optics

4.2.1. Preparing the Laser-Beams

This section gives only a brief overview of the lasers and used laser conditioning techniques. For more detailed explanations refer to [2]. For cooling the rubidium atoms in MOT/molasses and for the subsequent imaging we need one laser for cooling and imaging (“Cooler”) and another independent one for re-pumping (“Repumper”). The setup for our lasers is shown in Fig.(4.11). The cooler and imaging laser consists of a standard laser diode built in a commercial tapered amplifier (TA) “Topic” system with a power up to 1W. Since a laser diode has a linewidth of several GHz which is orders of magnitude higher than the natural linewidth of the rubidium transitions, we lower the broadness of the laser with an external grating [20]. Additionally we want to be able to tune the cooler laser freely within a certain range, to use it for MOT, molasses and optical pumping and to have room to optimize atom number and temperature of the trapped atoms. Optimization measurements are shown in Section 4.3.2. For this we use a frequency offset-lock [2]. With this technique we are able to set the laser frequency with a VCO by ± 70 MHz in respect to a reference frequency determined by a reference laser. The reference laser, called “Piere Luigi” in Fig.(4.11), is set by frequency modulation (FM)-lock to the crossover transition $5^2S_{1/2} | F = 2 \rangle \rightarrow 5^2P_{3/2} | COF = 2, 3 \rangle$, shown in Fig.(4.10). We chose this as our starting point because we want to use an acousto-optic modulator (AOM) for the final frequency shift to the cooling transition $5^2S_{1/2} | F = 2 \rangle \rightarrow 5^2P_{3/2} | F = 3 \rangle$. An AOM consists of a quartz crystal coupled to a piezo-electric transducer driven by a voltage signal. The piezo-electric transducer creates sound waves in the crystal which changes the index of refraction depending on the frequency of the sound wave. An incoming laser beam is then diffracted in an angle depending on the driven frequency [28]. By switching the driving frequency on and off we have the opportunity to switch the cooling light in below $1 \mu\text{s}$ which is much faster than it would be possible to switch with a mechanical shutter that switches in the order of ms. By overlaying an out-coupled beam from the Topic with the one from Piere Luigi we generate an error signal which is fed back to the Topic electronics to stabilize the Topic on the frequency chosen by the VCO frequency. All spectroscopies are measured by photo diodes (PD) or avalanche photo diodes (APD) for higher frequencies. The amplified laser beam (maximum power 940 mW) from the Topic is directly coupled into a fiber which leads to the MOT-optics described in the next section.

For the Repumper (“Rudi”) we use a standard distributed feedback laser diode stabilized by FM-lock. Here the power and linewidth of the laser diode is sufficient. We lock the laser on the $5^2S_{1/2} | F = 1 \rangle \rightarrow 5^2P_{3/2} | COF = 1, 2 \rangle$ transition to be able to shift it with an AOM to the re-pumping transition ($5^2S_{1/2} | F = 1 \rangle \rightarrow 5^2P_{3/2} | COF = 2 \rangle$). The stabilized laser beam has a power of 50 mW and is sent via fiber to the MOT-optics.

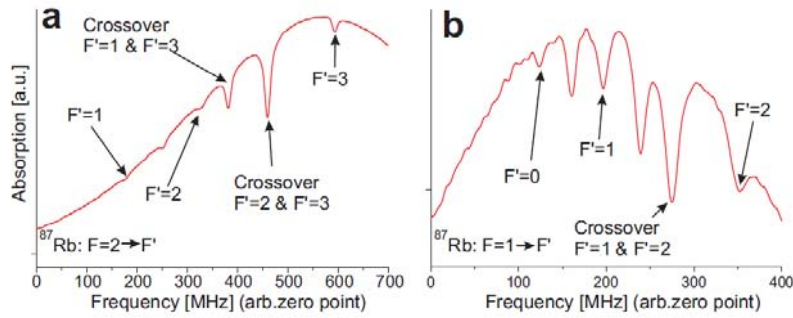


Figure 4.10.: Absorption spectrum of ^{87}Rb : a) Transition from the $5^2S_{1/2} | F = 2 \rangle$ ground states. $F = 2 \rightarrow F' = 3$ is the cooling transition, $F = 2 \rightarrow F' = 2$ is the optical pumping transition and we lock “Piere Luigi” to $F = 2 \rightarrow COF' = 2, 3$ b) Transition from the $5^2S_{1/2} | F = 1 \rangle$ ground state. $F = 1 \rightarrow F' = 2$ is the re-pumping transition and we lock “Rudi” to $F = 1 \rightarrow COF' = 1, 2$. Figure taken from [41].

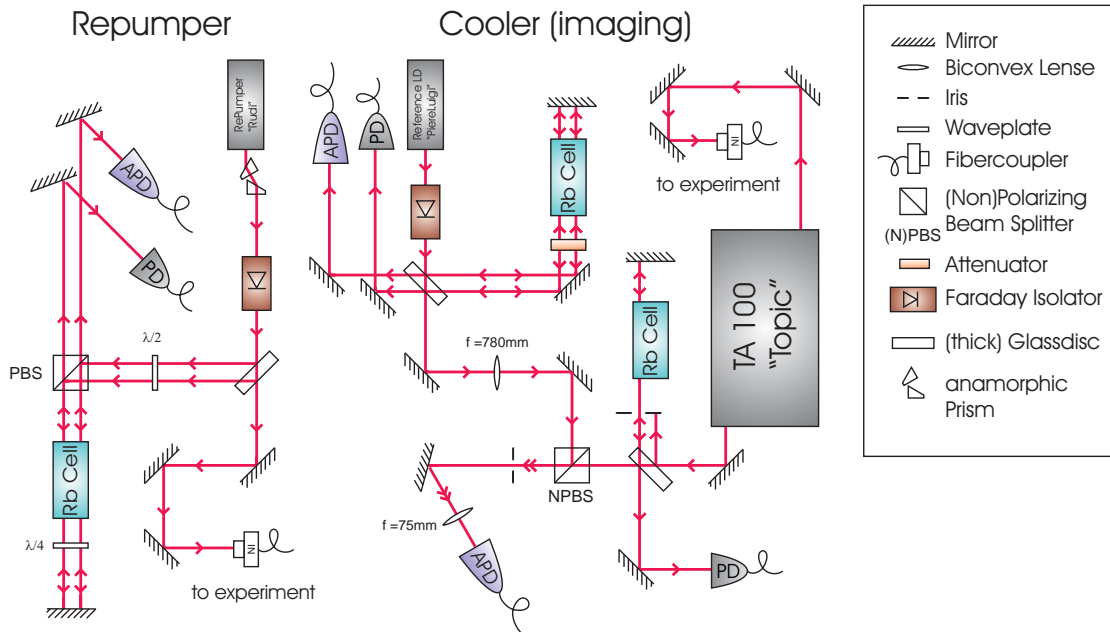


Figure 4.11.: Setup of the laser box for preparing the Cooler and the Repumper laser beam.

4.2.2. MOT- and imaging optics

Setup

As mentioned before we use AOMs to shift the lasers to the desired transitions and switch the light very fast (5 – 100ns). The AOMs used in our setup are fixed in frequency. The power of the diffracted beams depends on the angle of the incoming laser beam and the driver voltage. Fig.(4.12) shows the MOT-optics with the used AOM paths. The Cooler beam is diffracted by a 62.5 MHz AOM and we use the 0^{th} and the $+1^{st}$ order for our experiment. As Fig.(4.10) shows, we need to shift the laser frequency up to get from $COF' = 2, 3$ to the cooling transition $F' = 3$. Therefore we use the $+1^{st}$ order, which shifts the light 62.5 MHz up, for the cooling beam. Since we want to maximize the cooling power the AOM is adjusted to transmit maximum power into the first order. Tab.(4.3) shows the Cooler power measured at different stages of the optical path. We reach an efficiency of 67% for the AOM. After the AOM the cooling beam is split up twice by polarizing beam splitters (PBS), first for the cryo imaging and then for the imaging in the MOT chamber. PBS reflect vertical polarized light while horizontal polarized beams are transmitted. Since we don't need much power for the imaging beam (for imaging a power of a few mW is sufficient), and we want to lose as less cooling power as possible, we use a $\frac{\lambda}{2}$ -plate in front of the cubes to get the light horizontally polarized. After the second PBS we overlay in a third PBS the Cooling beam with the Repumper beam. The Repumper beam is also shifted by a 78.5 MHz AOM up to the re-pumping transition, using the same principle explained for the Cooler beam. The overlaid beams get widened to 1" in diameter by an optical telescope before they are further split up in 6 MOT beams of equal power. The power splitting is done with PBS and $\frac{\lambda}{2}$ -plates. Unfortunately we currently lose $\approx 20\%$ of the laser power after the telescope which should be possible to be lowered by readjusting. Finally the MOT-beams are polarized circular with $\frac{\lambda}{4}$ -plates in front of the MOT windows.

To get the right laser frequency for the pumping, we use the 0^{th} order of the cooling beam (which is not frequency shifted by the Cooler AOM). Fig.(4.10) shows that we need to lower the laser frequency to get from $COF' = 2, 3$ to the pumping transition $F' = 2$. We use a double pass AOM line to shift the beam by 2×81 MHz in the -1^{st} order. This results in a overall shift of -162 MHz to the pumping transition. After passing a PBS in horizontal polarization the beam is refracted by the AOM, passes a $\frac{\lambda}{4}$ -plate, gets reflected and passes the $\frac{\lambda}{4}$ -plate again which results in a polarization change from horizontal to vertical. After passing the AOM a second time the beam gets now reflected by the PBS and is coupled into a fiber. In our setup, the pumping beam is sent then through the same optics and window like the imaging beam. Therefore the polarization of the pumping beam can not be adjusted separately from the imaging beam because they pass the same $\frac{\lambda}{4}$ -plate. This leads to the problem that if one adjusts the pumping beam to pump the maximum atom number into the desired transport state it is impossible to get the image-polarization right. Hence we

	Cooler Power [mW]
after fiber	346
before AOM	285
after AOM	190
before cryo img PBS	187
after cryo img PBS	182
after MOT img PBS	175
before overlay cube	165
after overlay cube	145
before telescope	143
after telescope	114

Table 4.3.: The Cooler power measured at different stages of the MOT optics. We achieve an efficiency of 67% of the AOM and 80% of the telescope.

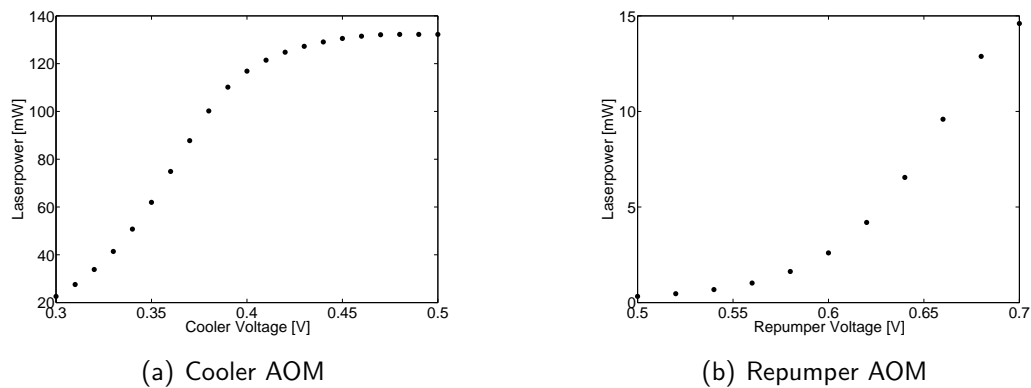


Figure 4.13.: The Voltage to Laser power conversion is highly nonlinear and different for every AOM and AOM-driver. The Figure shows the Laser power as function of the AOM-Voltage.

can't see the full atom number when imaging in the MOT chamber.

For characterization of the AOM paths we measured the laser power in the -1^{st} order of Cooler and Repumper in dependence of the input voltage (Fig.(4.13)). The conversion is highly nonlinear and different for every AOM and the corresponding AOM driver.

4.3. The MOT cycle

After preparing the laser beams for the MOT we align them to the center of the MOT chamber where the ^{87}Rb atoms are trapped. The MOT consists of different components: the laser beams, the MOT-coils, the compensation coils and the ^{87}Rb dispenser. Fig.(4.1) shows the MOT chamber included in the horizontal transport. Of course, the chamber has to be evacuated to a pressure in the order of 10^{-10} mbar to make a trapping possible. With a higher background pressure the atoms would be kicked out of the trap by collisions with background gas atoms. For sustaining the needed pressure there is a 50l/s ion pump connected to the MOT chamber. The dispenser provides us with the ^{87}Rb atoms by thermionic emission. The field of the compensation coils is adjusted to compensate the earth magnetic field and to provide a quantization axis for the magnetic moment of the atoms during pumping and imaging as shown in Section 4.1.2. Therefore the coil pairs that provide the magnetic field in x- and y-direction have fixed coil currents while we are able to change the current of the third coil pair, which provides the field component on the vertical z-axis, during the experimental cycle by the ADwin system (see Section 4.5). The current of the MOT coils is also controlled via ADwin.

An experimental cycle consists of three elemental stages: First, we trap atoms in the MOT, cool them and load them in a pure magnetic trap to prepare for transport. In the second stage we move the atoms with the magnetic transport into the cryostat or to a free selectable position and from there back to the cryo chamber. Finally we image the atoms in the cryostat or in the MOT chamber. This chapter describes the first and the last stage of the experimental cycle, while the Sections 3.3 and 4.4 deal with theoretical and experimental details of the transport.

4.3.1. MOT and magnetic trap

As described in principle in Section 3.1, we follow several steps for trapping and cooling atoms in the MOT and loading them into the magnetic trap. First we load atoms in a MOT with 6 laser beams and a magnetic quadrupole field created by the MOT coils. After a certain loading time, we switch the magnetic field off and increase the laser de-tuning for cooling the atoms in an optical molasses. Next we change again the detuning (while the magnetic field is still off) to get to the pumping transition. For loading into the magnetic trap the laser light is switched off and the MOT coils ramp up to a strong magnetic field that traps the atoms in a quadrupole trap. So the critical parameters for this process are the Cooler laser de-tuning and the magnetic field (or the current) in the MOT coils. A graph of the currently used times and values is given in Fig.(4.14). These are the optimized values according to the atom number in molasses or magnetic trap, which is shown in the next Section. Two things are to mention about this graph: First, the MOT loading time is decreased by a factor of 200 from 10s to 50 ms to make it possible to see all stages in one figure.

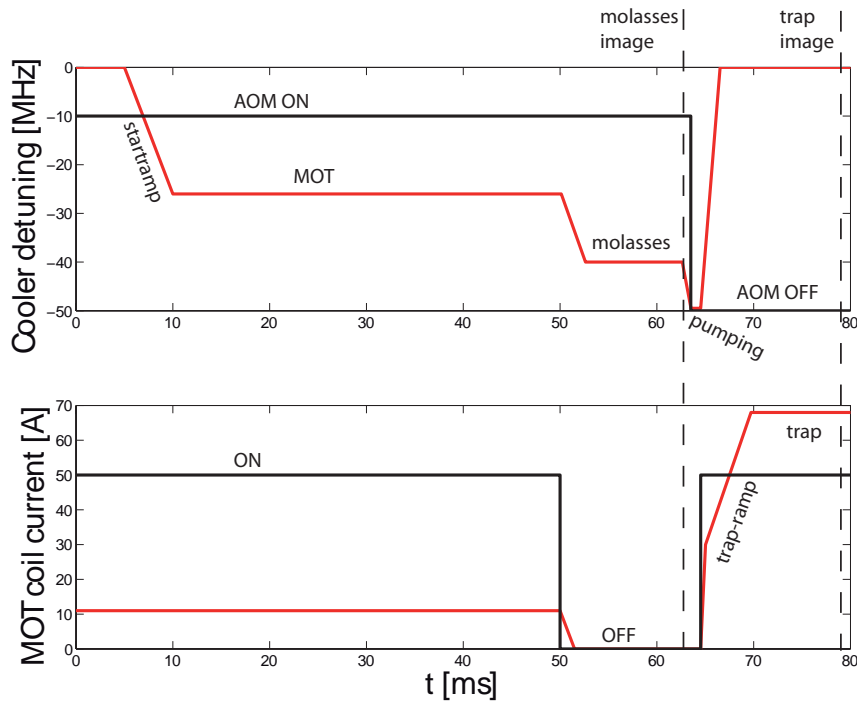


Figure 4.14.: The currently used MOT/trap cycle, analog signals of detuning and MOT coil current (red) and digital signals of the AOM and the MOT coils (black). The times for the different stages are: MOT-loading-time: 50 ms (reduced by a factor of 200 for graphical visualization); molasses-time: 10 ms; pump-time: 1 ms.

Second, one could think that the laser is off during the pumping stage, but since we use the 0^{th} order for the double pass pumping line we don't need the AOM to be switched on for getting the pumping beam, but we make shure that there is no light going through the MOT optics path.

4.3.2. Measurements and optimization

Detuning and B-field (gradient) of the MOT

We have two different ways of imaging and measuring atoms in the MOT chamber and characterizing our MOT and magnetic trap which are sketched in Fig.(4.14). For characterizing the MOT and molasses we image the atoms right after the molasses phase instead of loading them into the magnetic trap. Fig.(4.15) shows a plot of the measured atom number depending on MOT-detuning and MOT-current. (We used the same detuning in MOT and molasses for this measurement.) Lindquist

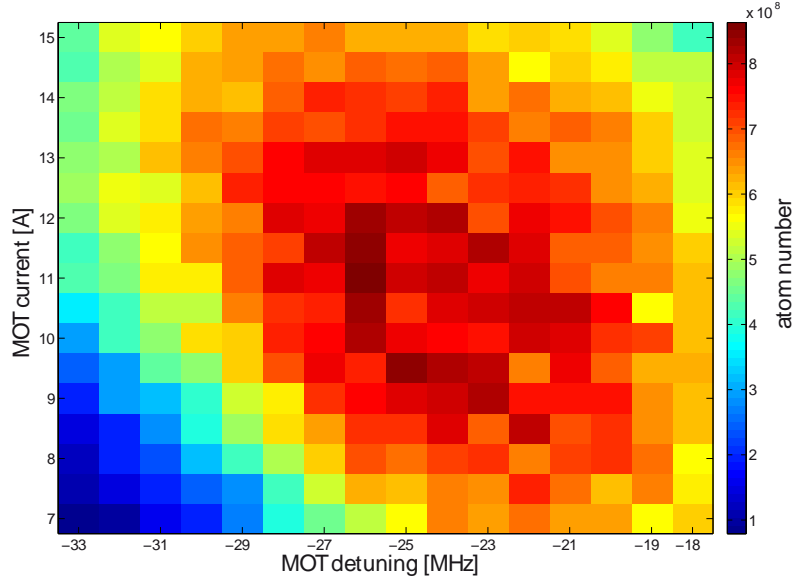


Figure 4.15.: The measured atom number in dependence of the current in the MOT-coils and the detuning of the MOT-light. From this measurement we chose $MOT_{det} = -26$ MHz and $I_{MOT} = 11$ A as optimized values.

et. al. [26] derived a model for a Cesium MOT which can help to understand this behavior qualitatively. Starting point for the calculations is the expression for the achieved atom number in an optical atom trap shown by Monroe et. al. [30]

$$N = R \cdot \tau = 0.1 \frac{A}{\sigma} \left[\frac{v_c}{v_{thermal}} \right]^4 \quad (4.4)$$

In this model the atom number is calculated by a ratio of a capture rate R and a loss rate $1/\tau$ due to collisions with the atoms of the background gas. The loss rate is proportional to the cross section σ for these collisions. The capture rate depends on the surface area of the trap volume A and the ratio $v_c/v_{thermal}$. v_c is the maximum velocity an atom can have to be still trapped while $v_{thermal}$ is the average velocity of the background gas atoms. $v_{thermal}$ can be approximated by using the energy relation for an ideal gas (Eq.(4.5)) and is in the order of 300 m/s for our MOT when we assume that the evaporated rubidium atoms from the dispenser have a temperature of about 400 – 500 K.

$$E_{kin} = \frac{mv^2}{2} = \frac{3}{2}k_B T \Rightarrow v = \sqrt{\frac{3k_B T}{m}} \quad (4.5)$$

v_c can be roughly estimated with a simple consideration. When we consider the

volume of the MOT one dimensional as a circle with 1 inch (2.54 cm) diameter we can calculate the absolute value of the magnetic field B_c at the border of the MOT section. The Zeeman energy $\Delta E = g_F m_F \mu_B B_c$ shifts the levels of the cooling transition ($5^2S_{1/2} | F = 2 \rangle$ to $5^2P_{3/2} | F = 3 \rangle$). Considering selection rules for an electric dipole transition ($\Delta m_F = 0, \pm 1$) the maximum frequency shift and therefore v_c can be calculated by Eq.(4.6). $\Delta\omega$ is the overall frequency shift which also corresponds to our chosen de-tuning δ by $\Delta\omega = 2\pi\delta$. $\Delta\omega_D = v \cdot k$ is the Doppler shift and $\Delta\omega_{B_c}$ the Zeeman shift.

$$\begin{aligned} \Delta\omega &= \Delta\omega_D + \Delta\omega_{B_c} = v \cdot k + \frac{2\pi}{h} \mu_B B_c \\ \Rightarrow v &= \frac{1}{k} (\Delta\omega - \frac{2\pi}{h} \mu_B B_c) = \lambda_L (\delta - \frac{1}{h} \mu_B B_c) \end{aligned} \quad (4.6)$$

With the undisturbed Wavelength $\lambda_L = 780.246$ nm, our chosen detuning in the MOT phase $\delta = -26$ MHz and a calculated $B_c = 15$ G, the result is $v_c = 36.65$ m/s. This means that we are only able to trap a low percentage of the evaporated atoms considering the atoms have a gaussian velocity distribution with a maximum at 400 – 500K.

Lindquist et. al. chose a different way to calculate v_c , stating it depends on a *radiation pressure force* F induced by the cooling light (For details about this calculation of v_c refer to [26]). Eq.(4.4), as well as the shown calculation for v_C considers only one room axis (v_C is a scalar). Lindquist et. al improve this simple formula for the atom number to find an expression valid in three dimensions in the MOT. They consider the trap volume as a cube with side L and state that the atom is moving in the x-direction. In their model v_C depends as well on the y- and z-axis because of the three dimensional magnetic field. They derive Eq.(4.7) for the atom number.

$$N = 0.1 \sum_{y=-L/2}^{y=L/2} \sum_{z=-L/2}^{z=L/2} \left[\frac{v_c(y, z)}{v_{thermal}} \right]^4 \frac{\Delta y \Delta z}{\sigma} \quad (4.7)$$

Next they derive an expression for the radiation pressure force F , considering the laser intensity, the laser de-tuning and the position dependent shift of the transitions resulting of the magnetic field. F leads then by integration to v_c and to an expression for the atom number. The results from this calculations are shown as black lines in Fig.(4.16).

If we compare this results to our measurements shown in Fig.(4.15) we see a qualitative match in the behavior. The calculated maximum from the Lindquist simulation is at about $-3.2 \cdot \Gamma_{Cs}$ with the natural linewidth of cesium $\Gamma_{Cs} = 5$ MHz, which gives a de-tuning of -16 MHz. We measured a value of -26 MHz for our MOT. ^{87}Rb has a natural linewidth of $\Gamma_{Rb87} = 5.9$ MHz, so this gives an ideal value of $-4.4 \cdot \Gamma_{Rb87}$. Considering the differences in the initial conditions, i.e. one has a different behavior in

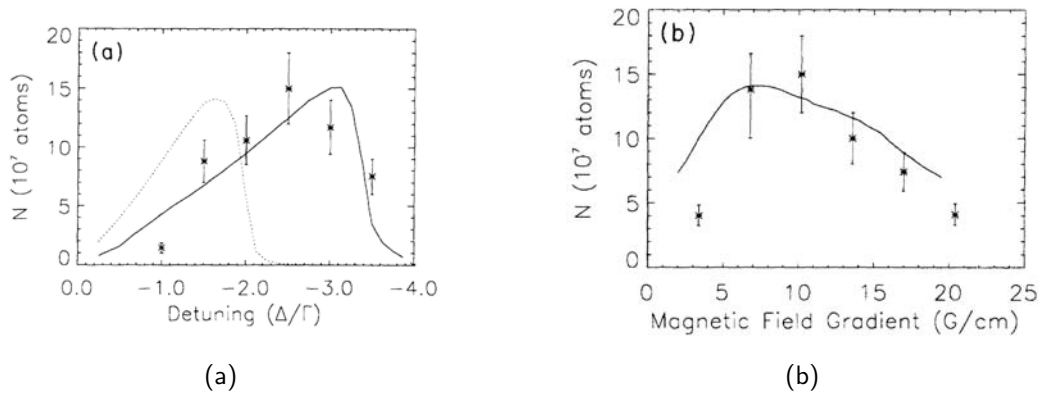


Figure 4.16.: Measurement results and calculations from Lindquist et. al. The black lines show the results from the simulations, the data points are the measured values from their experiment. The dotted line was calculated with a simpler, one dimensional model. Taken from [26].

the Zeeman splitting depending on the Zeeman levels of the used cooling transitions, our laser has a bigger diameter than the one used by Lindquist and the calculation depends on the intensity of the used laser beam, the match in number and behavior is quite remarkable. This shows that our MOT behaves just as expected and the behavior is in agreement with the shown theory.

However, the differences from the theory get stronger, when we have a look at the magnetic field gradient. As Fig.(4.16b) shows, the predicted ideal value would be about 7.5 G/cm while our measurements show a maximum for 11 A which corresponds to 23.67 G/cm. This is due to the factors mentioned above. Although the number differs by a factor of 3, the shape of the curve and therefore the principal influence of the magnetic field gradient on the atom number is similar.

From the measurement shown in Fig.(4.15) we chose $MOT_{det} = -26$ MHz and $I_{MOT} = 11$ A as optimized values.

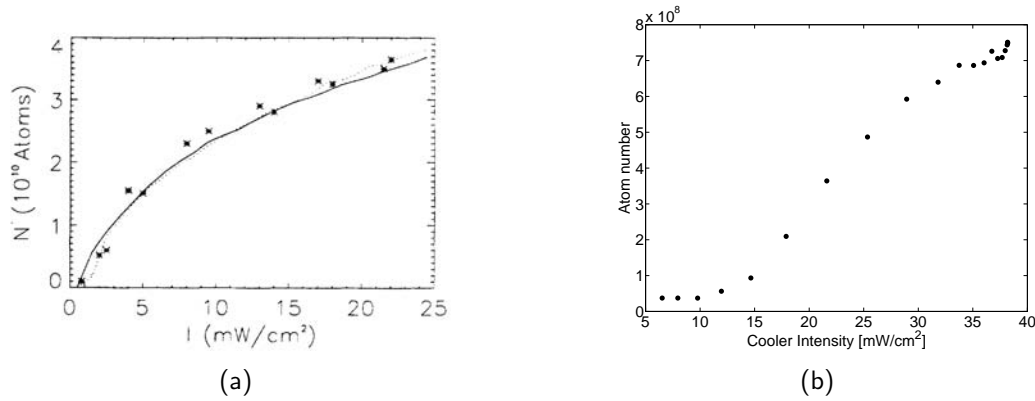


Figure 4.17.: Comparison between the Linquist model and data ((a)) and our measurements for the Cooler laser ((b)). The behavior is in qualitative agreement. For a better comparison one could have divided the intensity by the saturation intensity I_S which is $1.09 \text{ mW}/\text{cm}^2$ for the ^{133}Cs atoms [29] used by Linquist et. al and $1.67 \text{ mW}/\text{cm}^2$ for ^{87}Rb [38].

Influence of the laser power

With the Lindquist model it is possible to make predictions about the number of atoms as a function of the laser power. Fig.(4.17) shows how the calculated atom number depends on the beam intensity (power per element of area in the center of the beam) compared to our results obtained with the help of the AOM calibration curves shown in Fig.(4.13). Our measurements show a similar rising behavior with the difference that our curve seems to be shifted by about $13 \text{ mW}/\text{cm}^2$ to higher Intensities. So our number of trapped atoms starts growing at higher laser intensities. This may be the reason of the used laser beam diameter, which is 4 cm for Fig.(4.17a) compared to 1.54 cm in our experiment (Fig.(4.17a)). This is also noticeable in the absolute atom number which is about 2 orders of magnitude lower. From the shape of the curve which matches the calculated curve from the discussed model we can assume that we could improve the atom number in the MOT at least by a factor of 2 by using a higher laser intensity. The results for the repumper (4.18) show a saturation in atom number and don't leave space for improvement.

MOT loading time

The physics of the MOT loading procedure can be described with a simple birth-death-model shown in Eq.(4.8) [5].

$$\frac{d}{dt}N(t) = \alpha n_{cs} - \beta n_{cs}N(t) - \gamma N(t) \quad (4.8)$$

This model assumes that all the gain and loss processes are proportional to the stationary density n_{cs} which depends only on the dispenser current. The first term in

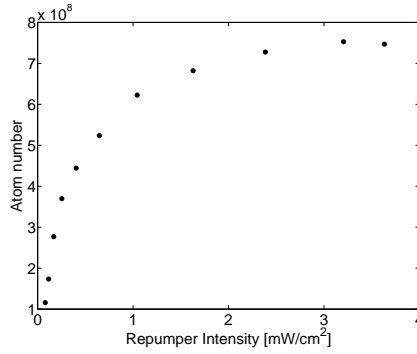


Figure 4.18.: The measured atom number for different repumper intensities. The curve saturates at 3 mW/cm^2 .

Eq.(4.8) describes the trap loading, α is proportional to the trapping cross section. The second term considers collisions between trapped and untrapped ^{87}Rb atoms while the third term takes collisions between trapped atoms and atoms of the background gas into account. Solving Eq.(4.8) leads to an exponential damped function which converges to the value A:

$$N(t) = A(1 - e^{-Bt}) \quad \text{with} \quad A = \frac{\alpha n_{cs}}{\beta n_{cs} + \gamma}; \quad B = \beta n_{cs} + \gamma \quad (4.9)$$

This is in qualitative agreement with our measured atom number vs. loading time curve plotted in Fig.(4.19). The rising follows not exactly the predicted shape, that's because we measured the atom number after loading into the magnetic trap for 50 ms. So additionally to the principle MOT loading procedure the loading phase into the magnetic trap influences the measurement results. We saw a rise of the atom number with the loading time which settles to a maximum in atom number after about 14 s. Since we want to meet a compromise between a fast cycle time and a high atom number we chose 10 s as optimal value.

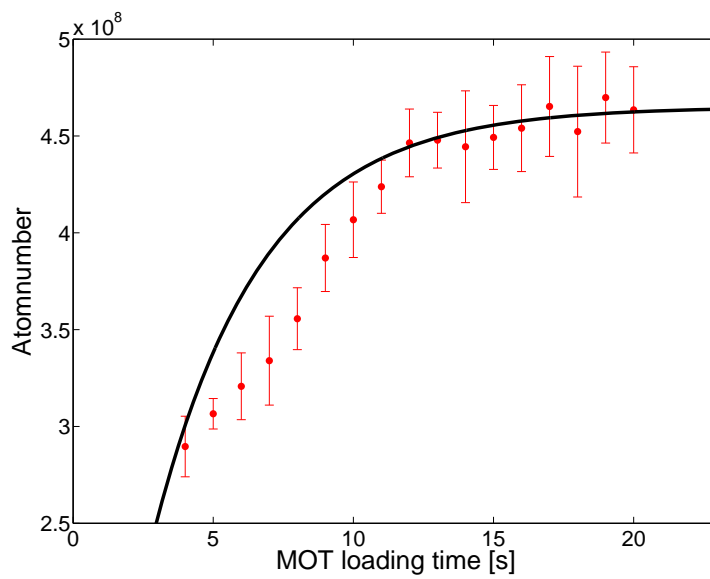


Figure 4.19.: The atom number depending on the MOT loading time measured in the magnetic trap (red). The black curve is a rough fit following Eq.(4.9) with the parameters $A = 4.65 \times 10^8$ and $B = 0.26$. The results follow qualitatively the predictions of the simple model. The measurement shows that a MOT loading time of about 14 s would be ideal. However, to meet a compromise between a high atom number and a low cycle time we chose a loading time of 10 s.

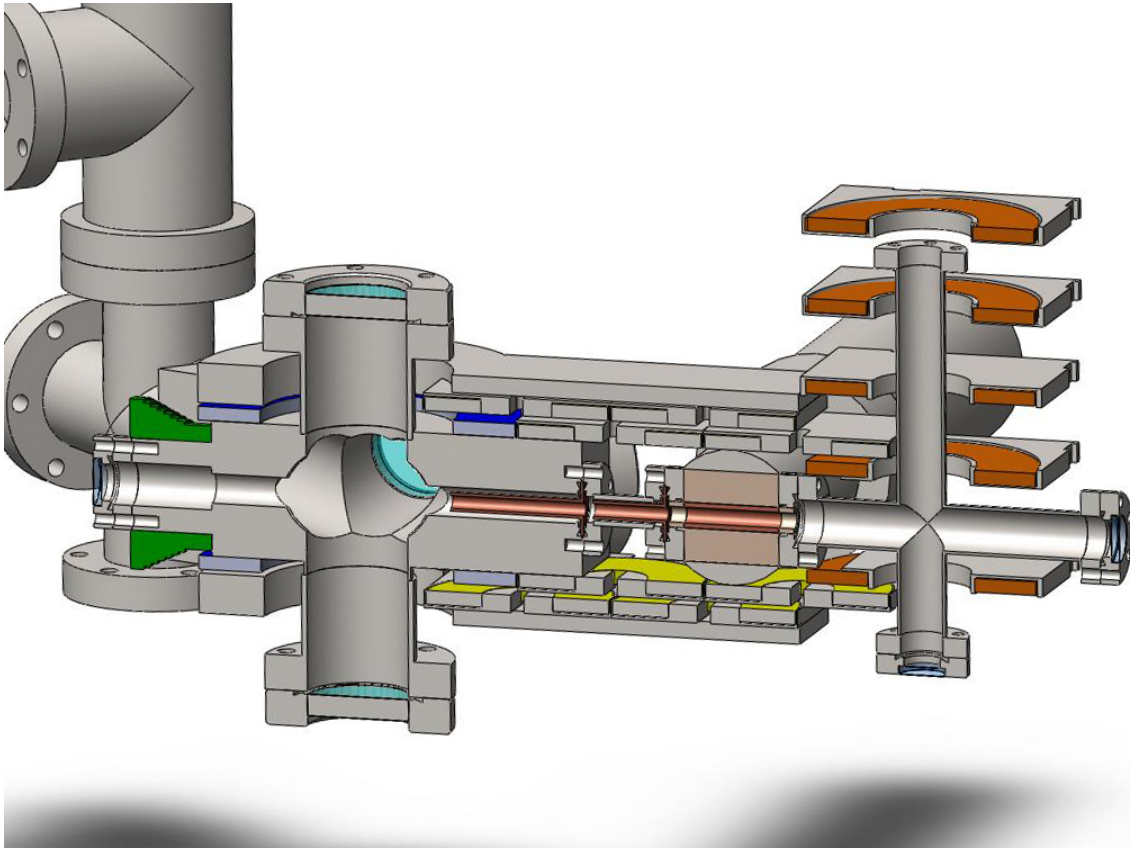


Figure 4.20.: Drawing of the normal conducting transport chamber.

4.4. The magnetic transport

As described in Section 3.3, our magnetic transport line consists of 16 normal conducting copper coils (including the MOT-coil-pair) [16] and 4 super conducting coils inside the cryostat. Since there is a big difference in manufacturing, mounting and driving of these two coil principles, I will discuss the realization of the normal conducting (NC) and the superconducting (SC) coils separately in the following sections.

4.4.1. The normal conducting transport

All normal conducting transport coils and the MOT coils are made of a copper wire with a rectangle-shaped cross section of 2.5×1 mm. The dimensions and number of windings of each coil are listed in Tab.(4.4). All normal conducting coils are driven by power supplies of the company *DELTA ELEKTRONIKA* and are able to provide up to 200 A. We use only 5 power supplies for the 11 different transport currents shown in Fig.(3.6) and Fig.(3.7) by switching the power supplies to different coils with self

made de-multiplexer boxes. Additionally, we use so called H bridges⁶ built into the de-multiplexer to be able to drive the current in both directions for the vertical coil currents. Since we are driving up to 120 A through the copper coils we need a water cooling system. We also monitor the coil-temperature via bi-metal sensors mounted on the coils which are connected to an emergency switch that cuts the power of all power supplies when reaching high temperatures.

4.4.2. The superconducting transport

Fig.(4.22) shows a drawing of the superconducting transport inside the cryostat. For the transport of atoms into the cryostat we had to invent superconducting coils and a cage for mounting and cooling them below T_C . We designed a cage made from high purity copper⁷ which is directly connected to the cooling finger. In the next section, I describe the manufacturing process and the engineering challenges we had to overcome for getting the superconducting coils to work. Tab.(4.4) shows the experimental properties of the superconducting coils. The coils are driven by current sources and polarity switches especially built by the electronics workshop. We need an “erasing circuit” to overcome the influences of the high inductivity (about 400 to 600 mH) when switching the coils off. The biggest problem is a fast switch off of a coil which induces a high induction voltage that could lead to a current flowing in the opposite direction of the primary current. This would make a measurement of atoms impossible, because the magnetic field would not disappear after switch off. Therefore we overcome this with an erasing circuit in the power supplies, which allows us to ramp the current to zero in 1 ms. More details and a circuit scheme of the coil switches can be found in [19]. As Section 5.1 shows, the described problem still occurred during the measurements, although we used the erasing circuits.

4.4.3. Superconducting Coils

For the transport into the cryostat we had to invent a new experimental approach for superconducting coils. While superconducting coils are usually cooled in a helium bath which keeps them below T_C , we had to find a liquid free cooling scheme to build the coils into the cryostat. We invented the copper coil cage shown in Fig.(4.22) that holds coil mountings made of the same copper. We use a wire that consists of a Cu-matrix with 54 niobium filaments (see A.1.2 for details). Niobium has a T_C of 9.2 K and when the wire is cooled under T_C all current is flowing over the Nb filaments. So the main task in manufacturing the coils and the cage is that the coils remain below T_C during operation. The cooling mechanism is only heat conduction via the

⁶An H bridge is a simple circuit consisting of 4 MOSFETs allowing to run current in two directions through a device under test (DUT). Details about the used H-bridges inside the de-multiplexer boxes can be found in [27].

⁷Oxygen free copper, reduced with Phosphor, purity ≥ 99.95 % (see A.1.1 for detailed specifications)

Normal conducting:

Coil	R_i [mm]	R_o [mm]	h [mm]	x [mm]	z [mm]	N_{axial}	N_{radial}	R[Ω]	$\frac{\nabla B}{l} [\frac{G}{A.cm}]$
PUSH	34	52...72	30.6	-56.65	0	12	6-13	0.102	-
MOT (pair)	36.2	59.5	5.1	0	± 27.5	2	23	0.023	1.07
H1 (pair)	13.3	34.3	5.1	60.5	± 34.22	2	23	0.0126	-
H2 (pair)	13.3	34.3	5.1	95	± 27.78	2	23	0.0126	-
H3 (pair)	13.3	34.3	5.1	129.5	± 34.22	2	23	0.0126	-
H4 (pair)	13.3	34.3	5.1	164	± 27.78	2	20	0.0126	-
V1	20	43	5.1	210.4	- 20	2	20	0.0115	-
V2	20	43	5.1	210.4	20	2	20	0.0115	-
V3	20	43	5.1	210.4	50	2	20	0.0115	-
V4	20	43	5.1	210.4	80	2	20	0.0115	-
V5	20	43	5.1	210.4	110	2	20	0.0115	-

Superconducting:

Coil	R_i [mm]	R_o [mm]	h [mm]	x [mm]	z [mm]	N	R_{300K} [Ω]	R_{5K} [Ω]	$\frac{\nabla B}{l} [\frac{G}{A.cm}]$
V6	24	35	5	210.4	140	3000	2065	0.4	-
V7	24	35	5	210.4	170	3000	2141	0.4	-
V8	24	35	5	210.4	200	3000	2142	0.4	4.15
V9	24	35	5	210.4	230	3000	2024	0.4	4.15
lofffe	5	10.5	8	-	230	1800	341	0.5	-
Super loffe	5.1	7.85	1.99	-	230	250	32	0.4	-

Table 4.4.: The transport coils for the magnetic transport. R_i , R_o and h are inner radius, outer radius and height of each coil, the position of the coils are given as x- and z-coordinates with the origin at the MOT position, N (or N_{axial} and N_{radial}) are the (axial and radial) windings of the coils and R gives the ohmic resistance of the normal conducting coils. R_{300K}/R_{5K} is the resistance measured from the outside at the normal conducting wires connected to a superconducting coil at room temperature and in the superconducting state. $\frac{\nabla B}{l}$ is the magnetic field gradient per Ampere in the MOT and in the superconducting quadrupole trap.

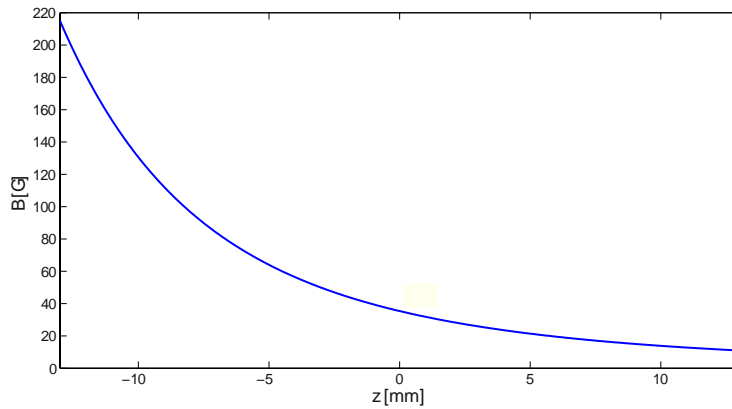


Figure 4.21.: Calculated magnetic field of the loffe coil along the coil axis driven with 1 A. The center of the quadrupole trap is at $z=0$. The position of the loffe coil is $z=-25.27$ mm.

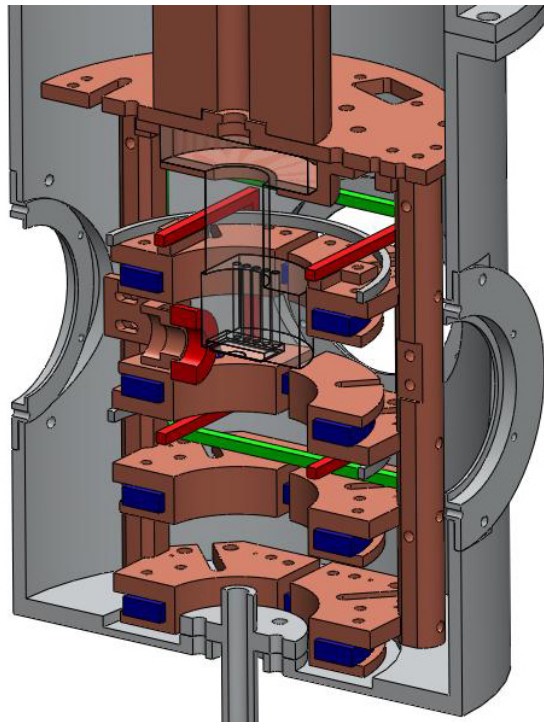


Figure 4.22.: Drawing of the superconducting coil mounting (4 K-cage) inside the cryostat. The transport coils (blue) are wound on special copper mountings connected by 4 copper rods to the 4 K-base. The loffe-coil (red [cylindrical shape]) is mounted on the side of the 4 K-cage between two rods. Additional BIAS-coils (green, grey, red [quadratic shape]) are planned to provide the BIAS-field for a Z-trap on the superconducting atom-chip. The planned chip-mounting for the atom-chip and/or a superconducting resonator is indicated in the center.

copper cage which is directly mounted to the cold finger of the cryostat. Therefore it is crucial to achieve good heat conduction between the copper coil mounting and the wire and between the coil cage and the coil mounting. It is important to press the parts, because the thermal conductance increases approximately linearly with pressure [11].

Fig.(4.23a) shows one of the first coil designs. The coil mounting is sliced to 4 parts to minimize the area of closed copper surfaces to prevent big eddy currents. The parts are connected with Stycast⁸, a strong two component epoxy which provides hardness, high thermal conductivity and electric resistivity. For winding the coils on the mounting and gluing the wire together we use GeVarnish⁹, an epoxy developed for use in cryogenic environments, which dissolves in ethanol. We use a GeVarnish/ethanol solution for wetting the wire during the winding process and drying it then at 80 °C for 12 hours to provide mechanical stability.

In the beginning we tried winding the coils directly on the copper mounting and fixing the 3000 windings with GeVarnish to the copper. With this method we always measured a short to the copper mounting when measuring the resistance after winding. To protect the windings, we attached a thin mylar foil¹⁰ with Apiezon N¹¹ as glue on the copper mountings before winding the coils, as can be seen in Fig.(4.23a). This worked well to isolate the wire from the copper mounting.

We also needed to invent a different design shown in Fig.(4.23b) because on the lowest coil position (V6) there is not enough space between coil and shield to build in the standard design. This second option has no “cap” and is therefore 5 mm lower in height (this results in an overall height of 10 mm compared to 15 mm of the first design).

Getting the coils superconducting

In the first measurements with coils mounted in the cage and cooled down to about 5 K in the cryostat, we encountered two different types of problems: First, the coils or at least the wire itself, stayed at a temperature above T_C and didn't get superconducting which means that somehow the cooling mechanism and the heat transport did not work properly. We measured then a resistance of about 25 Ω on the coil connectors compared to 0.5 Ω when they got superconducting. Second, the coils got superconducting, but when applying a current to it, it couldn't sustain the current and eventually got destroyed.

After several measurements with different coil generations we realized that the coils are facing directly the optical windows of the 77 K shield as can be seen in Fig.(4.22). A temperature measurement of the shield and the windows lead to the conclusion that while the shield was on a temperature of 55 K, a sensor mounted in the middle of

⁸Stycast Type 2850FT/11

⁹GeVarnish IMI-7031

¹⁰0.025 mm thick mylar ICEles40 from ICE Oxford

¹¹Apiezon N vacuum grease, Apiezon Products, www.apiezon.com

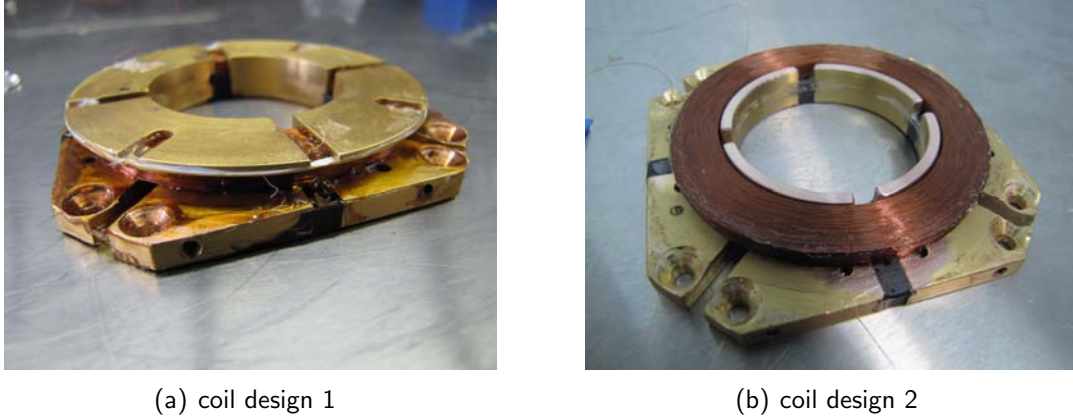


Figure 4.23.: The two coil designs used for the superconducting transport coils.

a window was on 146.8 K. The thermal conductance between shield and window was according to this results very bad and the coils wire was directly facing a surface with 146.8 K in a distance of 30 to 50mm depending on the coil. A rough calculation using the Stefan-Boltzmann for heat transfer by radiation between two surfaces (Eq.(4.10)) leads to a heating power by radiation of 0.18 mW. (With the Stefan-Boltzmann-constant $\sigma = 5.67 \times 10^{-8} \text{ W}/(\text{m}^2\text{K}^2)$, the emissivities of glass for the window ($\epsilon_g = 0.9$) and of copper for the coil wire ($\epsilon_c = 0.02$), the area $A = 350 \text{ mm}^2$ of the coil exposed to the radiation and the temperatures of the surfaces $T_g = 146.8 \text{ K}$ and $T_c = 5 \text{ K}$) [11].

$$\dot{q}_{rad} = \sigma A(T_g^4 - T_c^4) \frac{\epsilon_g \epsilon_c}{\epsilon_g + \epsilon_c - \epsilon_g \epsilon_c} \quad (4.10)$$

To shield the wire from the radiation coming from the windows we used aluminium tape. Fig.(4.24) shows a picture of the shielded coils. In the subsequent cool-down with this shielding all coils got superconducting and stayed ever since.

When we measured a resistance of about 0.5Ω on the coil wires, we had to test if we can drive them with a current of 1.5 A maximum. We need a current of about 0.8 A (as Fig.(3.7) shows) for the transport and we want to have some headroom to be able to make the quadrupole and quadrupole-loffe trap steeper. In first tests we noticed that some coils suddenly heat up and even loose superconductivity at a certain current. Fig.(4.25) shows an example of such a behavior. It shows a current measurement where we increased the current through a coil slowly and measured the temperature with 3 sensors. It was done with an earlier generation of coils, for simplicity named coil 1 (blue) and coil 2 (red). There was no specified difference in those two coils, they were built in design 1 and mounted and soldered in the same manner. Sensor A is mounted on the upper baseplate ("4K-base") of the coil cage directly connected to the cryo-finger, Sensor B is mounted on the red coil and Sensor C is mounted on

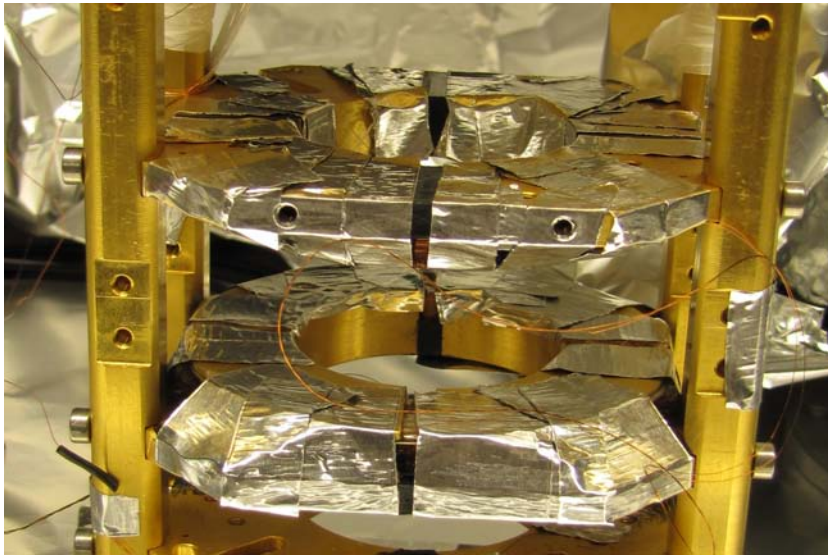


Figure 4.24.: The aluminium tape shielding of V8 and V9 to prevent the wire being heated from the windows.

the blue coil. The sudden heat up (which goes hand in hand with a rise in resistance) of the red coil starts at 0.8 A. We discovered that if we hold this current constant when the heating starts, the resistance rises until we lose superconductivity. We assumed that the reason for this behavior is a heating on the solder contacts from the superconducting wire of the coils to the normal conducting wire down to the 4 K-base. In the normal conducting wire the current induces heating and a solder joint is generally the best thermally conducting interface [11]. Therefore, it is crucial to thermally anchor the normal conducting wire very well on the 4 K-base to get rid of all produced heat before it heats up the superconducting wire. Additionally, the solder contact itself could produce heat and so it is also important to anchor the superconducting wire after the solder contact very well to the 4 K-base. It is well known that, if the wire is not anchored well, a certain current induces heating in the superconducting wire which leads to a rise of the resistance which leads again to a heating and so on. This would describe the observed behavior shown in Fig.(4.25). Therefore we tried different methods of soldering and anchoring of the wires on the 4 K-base. At first, we did a simple lead¹²-containing solder¹³ contact of 1 to 2 cm length isolated with a heat shrink tube and taped the wires with aluminium tape down on the 4 K-base. As we observed the described behavior, we implemented two additional features to improve the soldering contact and the anchoring. We improved the solder contact with a copper tube which was filled with solder to maximize the contact area and we wound the superconducting wire several times around small copper pillars which were mounted on the 4 K-base. With these measures we could prevent

¹²lead has a T_C of 7.9 K and should therefore be superconducting at the described conditions

¹³Solder of type: HF32, S-Sn60Pb39Cu1

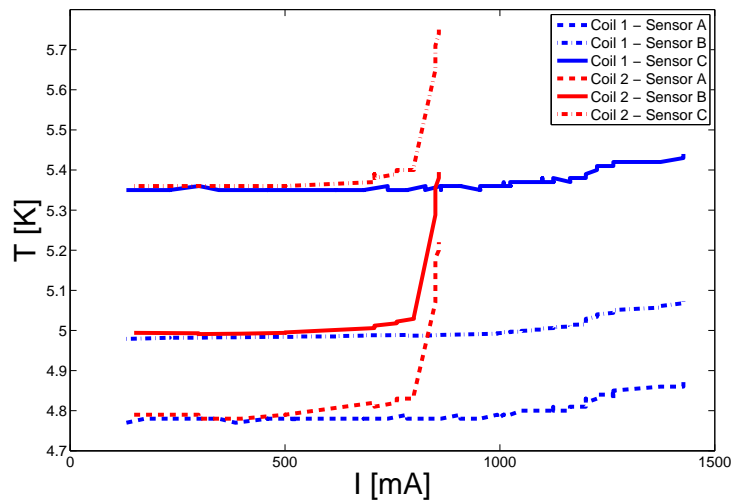


Figure 4.25.: The observed sudden heating in the superconducting coils when increasing the coil-current. We measured the temperature of the system with three different sensors, Sensor A mounted on the 4 K-base, Sensor B on coil 2 (red) and Sensor C on coil 1 (blue). While Coil 1 shows only a slightly increase in temperature at currents over 1 A, Coil 2 starts suddenly to heat up quickly at about 0.8 A.

this sudden heating and managed to drive 1.5 A through each of the superconducting coils.

4.4.4. The 4K-cage

Fig.(4.26) shows an up to date picture of the 4 K-cage. Inset (a) shows the described soldering method, the copper pillars in the background and one soldering contact with a copper tube inside a black insulation tube in the front. One can also see the aluminium tape to anchor the wire on the baseplate. Inset (b) is a charcoal container for additional passive pumping power to improve the vacuum, this is discussed in detail in Section 5.1. Inset (c) shows the mounting for the loffe-coil. The properties of the coil are listed in Tab.(4.4). We built in an additional coil, called “Super loffe”, on top of the loffe-coil to have the possibility to shift or modify the quadrupole-loffe trap independently. The loffe-coil and the super loffe-coil are shielded with aluminium tape like the transport coils against the thermal radiation from the windows. For the first goal to cool down to a BEC by evaporative cooling we built in a normal conducting RF-coil (red coil in the center of Fig.(4.26)) wound on a copper blinding which additionally shields the coils from direct exposure.

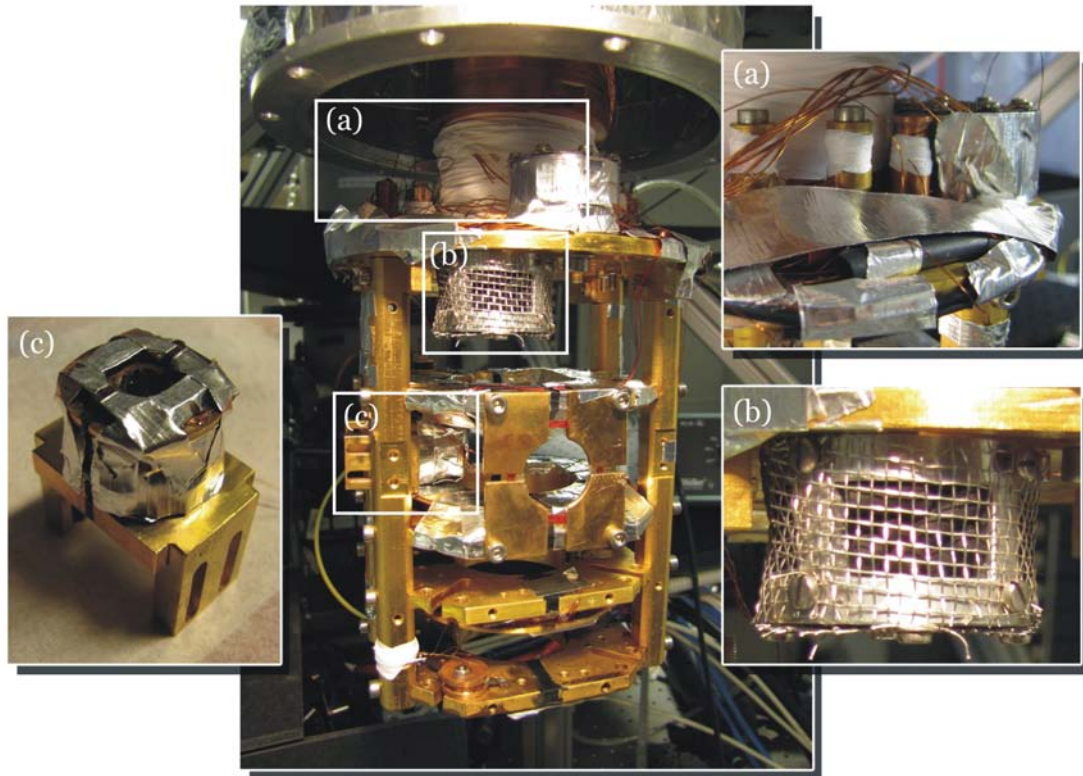


Figure 4.26.: The actual setup of the 4 K-stage. (a) shows the anchoring of the superconducting wires on the copper pillars, the wire is wound around the pillar several times and fixed with Teflon tape, and in the front a copper tube soldering (visible is only the black insulation tube) with the wires on both sides of the contact taped to the 4 K-base. (b) The containers for charcoal-pellets built from high quality aluminium. In this particular container, we built in windows to maximize the pumping surface of the pellets in direct contact with the surrounding. (c) The copper mounting for the loffe and Super-loffe coil to fix the coils in between V8 and V9. The Super-loffe was simply glued with on top of the loffe coil with GeVarnish. Both coils were isolated with aluminium tape to shield the thermal radiation.

4.5. Experimental Control

We use a commercial “ADwin pro” system from the company *Jaeger Messtechnik*¹⁴ for experimental control. The ADwin hardware consists of 4 “Aout 8/16” modules which provides us with 32 analog output channels with a signal range from -10 to 10 V and 2 “ADwin Pro DIO 32” modules with 32 digital channels each, which gives us a total of 64 digital output channels. The digital channels give out 0V for “0” and 5V for “1”.

All elements that need to be controlled during an experimental cycle are connected to the ADwin system, including the laser detuning of the cooler laser via the VCO of the cooler master, the AOMs, the MOT-, transport- and compensation-coils, the laser shutters and the camera trigger for both imaging cameras. For the analog signals that are used to control the current sources of the coils we use isolation amplifiers to minimize the noise and prevent ground loops. The ADwin system itself is grounded only via the signal cable to the laser VCO of the cooler master to make sure we have a defined ground and at the same time no ground loops. The hardware is connected via ethernet to the control PC. Fig.(4.27) is a schematic of the used devices and connections.

The software that controls ADwin is written in Jaeger's own programming language “ADbasic” which includes direct commands to access the hardware. We use a Matlab environment for a graphical user interface (GUI) and the experimental cycle programming, which sends our data via an ADbasic script to the ADwin hardware. Analog channels are controlled via arrays with 2048 values per channel. An analog signal for ADwin is defined by discrete values x at defined time-points $t^{(m)}$ (the index m stands for the m -th time-point), and a polynomial function which defines the behavior of the signal between the points $x(t^{(m)})$ and $x(t^{(m+1)})$ (Eq.(4.11)). Up to a third degree polynomial ($n = 3$) is possible.

$$p_{x_n}(t) = \sum_{i=0}^n a_i^{(m)} (t - t^{(m)})^i \quad \text{with} \quad t^{(m)} < t < t^{(m+1)} \quad \text{and} \quad a_0 = x(t^{(m)}) \quad (4.11)$$

For the program these polynomials are defined by 8 entries in an array in the following format:

...	n + 1	t ^(m)	a ₀ ^(m)	a ₁ ^(m)	a ₂ ^(m)	a ₃ ^(m)	0	0	...
-----	-------	------------------	-------------------------------	-------------------------------	-------------------------------	-------------------------------	---	---	-----

Each of this entries define a starting point $x_m = x(t^{(m)})$ and a polynomial function $p_{x_n}(x_m, t)$ which describes the curve to the next step x_{m+1} . Since each step needs 8 entries, we have 256 possible steps for one analog channel. For the values $x(t)$

¹⁴www.adwin.de

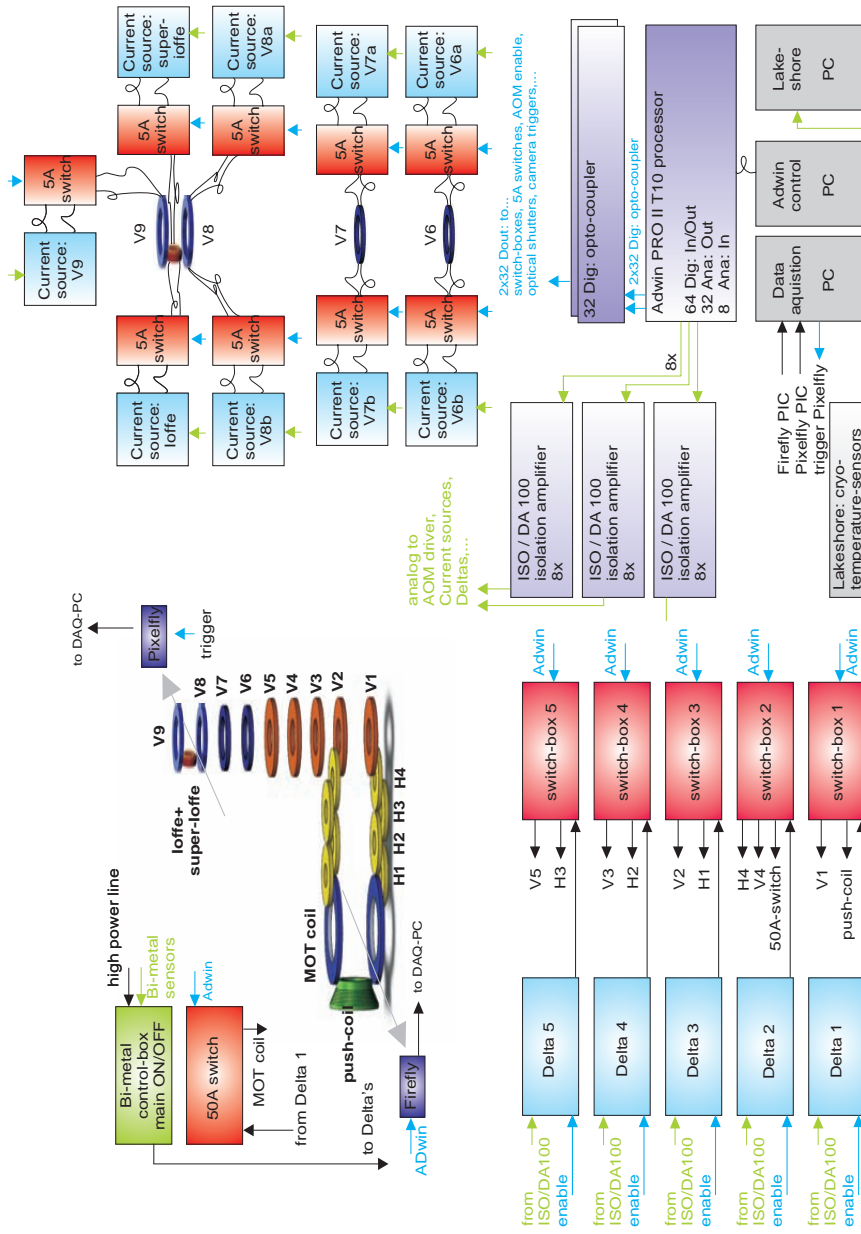


Figure 4.27.: The connections and elements of the control setup. The whole system is secured by Bi-metal temperature sensors connected to a control box which switches all Delta supplies off when the temperature of the coils exceeds 70 °C (green box). The current of the MOT coil is switched by an extra 50A switch (red box on the right). The normal conducting coils are connected via switch-boxes to the Delta power supplies, the switch boxes and the Delta supplies are controlled by ADwin. The superconducting transport coils V6, V7 and V8 are connected to two current sources with a 5A switch for driving the superconducting transport currents in both directions (as shown in Fig.(3.7)). For the normal conducting vertical transport coils (V1 - V5) this is done by the use of H-bridges inside the switch-boxes. V9, the loffe coil and the super-loffe coil are connected to only one current source and switch because only one polarity is needed. All analog signals for the current sources are isolated from ground via DA 100 isolation amplifiers. We use three different PC systems, one for data acquisition of the camera images and controlling the camera, one for the ADwin control described in this section and one for measuring the temperature in the cryostat with a Lake-shore sensor system.

ADwin uses half-precision words (16-Bit) as resolution, therefore 0 corresponds to -10V and $2^{16} = 65536$ corresponds to 10V .

For the digital channels ADwin needs only time information to switch from 0 (0V) to 1 (5V) and vice versa, nevertheless ADwin uses also a 8 entry format for each time step comparable to the analog solution:

...	s	$t^{(m)}$	$v^{(m)}$	0	0	0	0	0	...
-----	-----	-----------	-----------	---	---	---	---	---	-----

s is 1 if there is information sent to ADwin, and zero if the block is not used and could therefore be ignored. $t^{(m)}$ is a time value in the same format as for the analogue channels. $v^{(m)}$ is a single precision number which holds the information for 32 digital channels in 32-Bits, each Bit corresponding to a digital value. If one channel changes the value, the time of the change is written to $t^{(m)}$, ADwin flips the Bit corresponding to the channel and sends a changed $v^{(m)}$ to all digital channels. It uses 2048 entries for 32 digital channels which allows to use 256 different time steps for one cycle. Since we have 64 digital channels, we use $2 \cdot 2048 = 4096$ values for the digital channels. It is important to note that even when we have different areas for storing the values of the first 32 channels and the second 32 channels, we still have only 256 possible time values since every time point produces an 8 part entry in each of the 2048 part arrays. This seems to be a historic issue, since the system was running on 32 digital channels in the beginning and was then upgraded to 64 channels.

For the ADwin commands we store all Channel-data in one big 1-D array. First the analog channels (channel 1 in the slots 1 to 2048, channel 2 in slots 2049 to 4096 and so on), which makes a total of 65 536 entries. After that, the 4096 entries for the digital channels are put in. This produces an array with the overall size of 69 632. We use a time resolution of $25 \mu\text{s}$ for the internal ADwin clock. Time values $t^{(m)}$ have to be given in μs divided by 25, this means that the values given to ADwin are the number of internal timing runs.

So for an experimental cycle we have to fill this ADwin array with the control signals for our experimental elements. Most of the MOT and imaging elements (AOMs (laser power), shutters, the VCO (laser detuning), cameras) are controlled via the GUI and can be changed independently from each other. For analog channels it is possible to set consecutive $x(t)$ values and choose whether to keep them constant and make then a sudden step to the next value or to ramp linear up to the next value. In the GUI it is possible to set 16 points or ramps. For digital channels we can set 16 switch-times. More details about ADwin and the Matlab GUI can be found in [33] and [7].

For the transport we need to implement the $I(t)$ curves calculated in Section 3.3. Since some of the calculations are already done in Matlab we generate arrays in the ADwin format corresponding to the current curves and write them directly in a big array which is sent to ADwin. This is the crucial part for controlling the magnetic transport and is described in detail in the next section.

4.5.1. The transport currents in ADwin

In Section 3.3 I explained the theory behind the calculations for the transport coil currents. The first step was the calculation of $I(x)$ and $I(z)$ curves. This was done analytically in *Mathematica*, then the curves were numerically imported into Matlab and fitted with a spline function. This was done for every coil current and the fitted splines were saved to a Matlab container called *stromfits.mat*. This container is the main source for the coil-currents, and it is imported in *startstop_main_control.m* which is executed when the experimental cycle is started via the GUI.

The next step is to calculate time values for chosen positions of the trap, depending on the transport parameters needed for the time calculations. These are x_{final} , T and T_{max} for the horizontal transport and z_{final} , v_0 and a_{max} for the vertical part as explained in Section 3.3. We can enter these parameters directly in the function *magnetic_transport_parameters.m*. The calculation program follows for horizontal and vertical the same principle although the physical calculations are different.

First we calculate $x(t)$ and $z(t)$ curves analytically. This is done for the horizontal transport in *ort_von_zeit.m* and for the vertical part in *zeiten_berechnen.m*. To find a good compromise between precision of the $I(t)$ curves and the speed of the calculation we chose to split each coil current curve in 16 regions with the splitting points x_1, x_2, \dots, x_{16} and fit the areas in between with spline functions which are finally converted to ADwin polynomials. This splitting is illustrated for the Coil-pair H2 in Fig.(4.28). The splitting points are saved in the data files *orte_hor.dat* and *orte_vert.dat*. They are read in by the programs mentioned above and with the calculated $x(t)$ and $z(t)$ curves we can find a time value to each splitting point. They are stored in an global ADwin array called *adwin.magnetic_data.zeiten* (horizontal) and *adwin.magnetic_data.zeiten_vert* (vertical).

Since we have to consider a transport back, which would involve the reversed current curve, we calculate also time values for the back transport stored in *adwin.magnetic_data.zeiten2* and *adwin.magnetic_data.zeiten2_vert*.

For finally calculating the current value to each time point, fitting a 3rd degree polynomial in between them and writing this results into the ADwin format, we use the function *anadwin.m*. This function is executed for every coil-current and has several input parameters. The most important are the time-points (“zeiten”), x_{final} or z_{final} , the positions (“orte”), the current spline from *stromfits.mat*, a “ramphight” and “ramptime” for pre-ramping the power supplies and a current conversion factor for the used power supply.

We discovered that the DELTA power supplies are not able to follow exactly the current curves when starting the curve at 0 A. Therefore we pre-ramp the supplies to a small current (200 mA, which is set in the ramphight parameter) with a ramptime of 10 ms. With the use of this trick the supplies follow the afterwards applied current

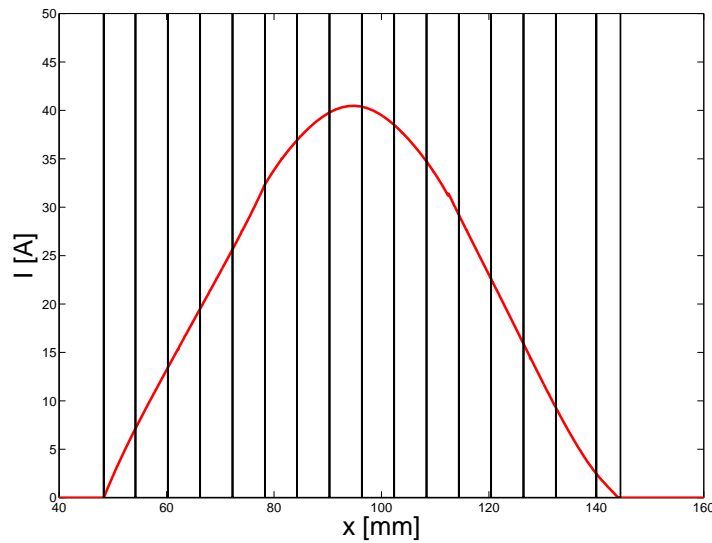


Figure 4.28.: An example how the current curve is sliced to 16 regions for the H2 current.

curves precisely. The current conversion factor is the conversion from the current to the desired ADwin output voltage and depends on the used power supply. While this factor is constant for the commercial DELTA power supplies, it is varying for our self manufactured power supplies for the superconducting coils and has to be measured separately for each used supply. The variation of one conversion factor to another is about 3%.

As explained above, *anadwin.m* calculates $I(t_1), I(t_2), \dots, I(t_{16})$ and the 3rd degree polynomials in between by using the input parameters and Matlabs fit routines. Additionally, it calculates $I(t)$ values for the transport back if this option is chosen in *magnetic_transport_parameters.m*. It outputs then an array for every coil in ADwin format. *startstop_main_control.m* calls *anadwin.m* for every coil-current and the arrays are stored in the global struct *adwin.magnetic_data*, for example the array for H2 in one direction is saved into *adwin.magnetic_data.H2_1*.

4.5.2. The digital transport channels

Additionally to the current-control-signals for each power supply we need signals to switch the supplies on or off and also switch the de-multiplexer boxes to the actual used coils. *startstop_main_control.m* executes the function *set_digital_values.m* which runs *calc_digital_adwin_data.m*. These two functions simply read out the values set in the GUI and convert them to an ADwin array. Moreover, *calc_digital_adwin_data.m* runs *digital_splines.m* which is the program where the digital values for the trans-

port are generated. The digital channels are calculated with 5 different functions, one for the MOT coils (*digital_MOT.m*), one for the normal conducting coils (*digital_normal.m*), two for the coils in the corner for the switch from horizontal to vertical transport (*digital_V12.m* and *digital_V2.2.m*) and finally one for the superconducting coils (*digitalSuperV.m*). This is necessary since we have to meet different conditions for these cases. For example, the MOT coil signal is a combination from the values set in the GUI for the MOT, molasses and magnetic trapping phase and the calculated times from the transport. These functions use (of course) the same input parameters than *anadwin.m* and give back the times into a global array *adwin.spline_switch_times*. It has already the size of 4096 needed for ADwin and has entries for the digital channels used by the transport. In *calc_digital_adwin_data.m* it is added up with an array resulting from reading out the GUI entries and put into the final global array *adwin.data_2* on the positions 65 537 to 69 632. This means *adwin.data_2* is ready to be sent to ADwin, but before that the analog values have to be entered.

4.5.3. Sending the data to ADwin

Just as it is done in *calc_digital_adwin_data.m* for the digital channels, the function *calc_analog_adwin_data.m* reads out the entered values from the GUI into the *adwin.data_2* array. In *testloop.m* the function *calculate_splines.m* is executed which combines the coil currents stored in *adwin.magnetic_data* to arrays with 2048 entries for each channel. This needs to be done because we sometimes use one power supply, which is controlled by one analog channel, for different coil-currents as described in Section 4.4. Then the resulting arrays are added up to the right position in *adwin.data_2*.

With this step we have reached an array with 69 632 elements which contains all data from the GUI and from the transport calculations for 32 analog and 64 digital channels which is finally sent via a compiled script written in ADbasic to the ADwin hardware. Fig.(4.29) is a flow chart of the used functions for the transport.

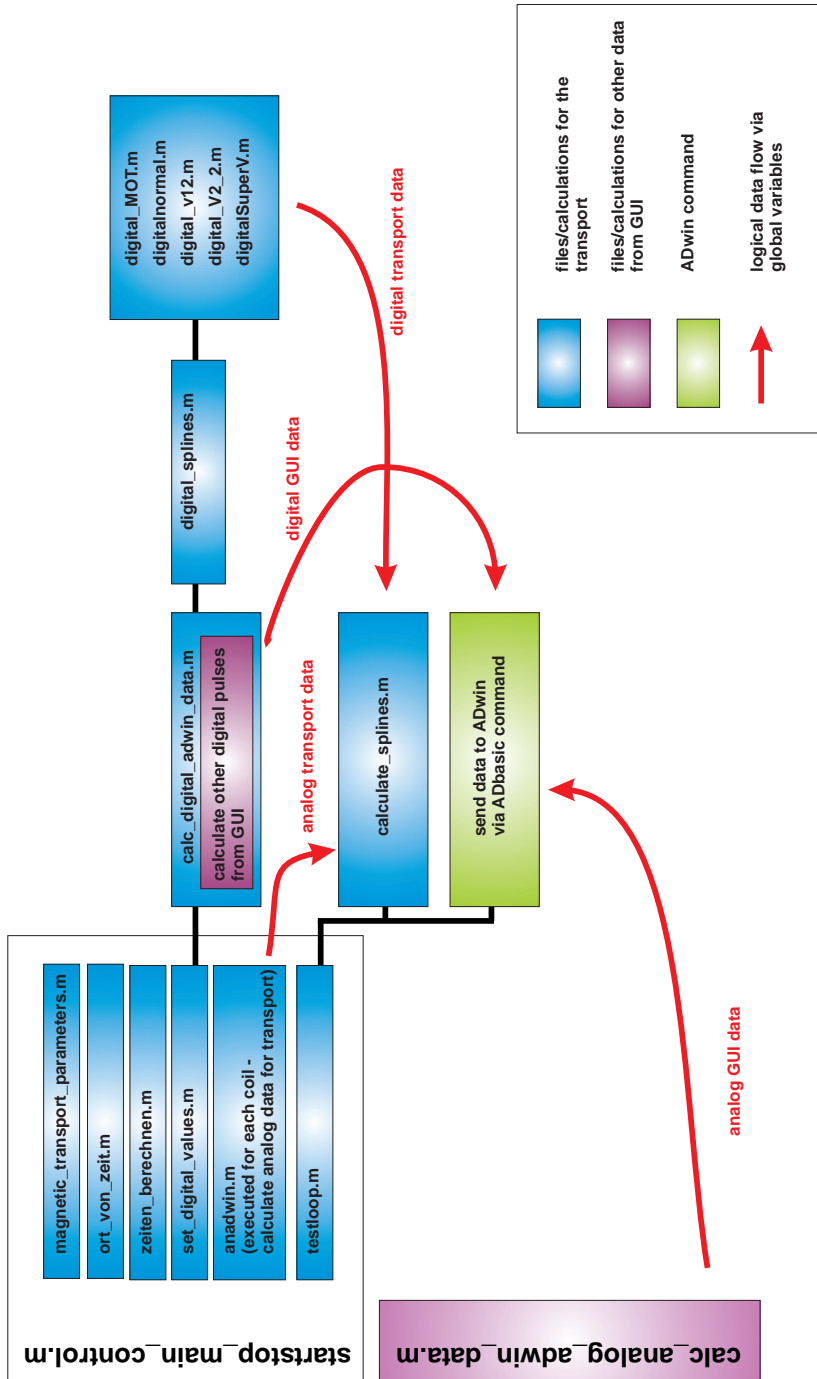


Figure 4-29.: A flow chart of the described Matlab functions used for the transport. The logical order is from up to down and left to right. This logical structure is integrated in the bigger programming structure of the experimental control system. Details about the general experimental control can be found in [33] and [7].

Part III.

Results: Atoms in the cryostat

5. Results: Atoms in the Cryostat

5.1. Atoms in the quadrupole Trap

One of our first achievements after solving all engineering challenges was the transport of the atom cloud into the cryostat, holding it in the quadrupole trap generated by V8 and V9 and take an absorption image. Fig.(5.1) shows an in situ image which is taken after holding the atoms 50 ms in the trap. We calculated the atom number by averaging over 80 images to $N_{av} = 1.00 \pm 0.07 \times 10^7$. The atom cloud is vertically elongated because of the ratio $dB_z/dz : dB_x/dx = dB_z/dz : dB_y/dy = 2 : 1$ for an anti-Helmholtz coil pair. The size of the cloud is about 2×2 mm.

To measure the temperature of the atoms we tried to make a time of flight (TOF) measurement. In these measurements we switch the magnetic trap off as fast as possible, wait for a certain time and make then the absorption image. During this time of (free) flight the atoms feel no force except gravity and reshape to an expanding spherical shape with gaussian distribution due to the gaussian velocity distribution in a thermal cloud [1]. By measuring the broadness of the distribution at different TOFs one can calculate the mean velocity of the atoms and therefore the temperature [12].

But when we increased the time of flight the atoms “vanished” after a time of approximately 2 ms as can be seen in the lower part of Fig.(5.2). However, when we increased the time of flight further we could see atoms again and noticed an oscillatory behavior in the measured atom number. The reason why we couldn’t see the atoms must have been a change in the absorption behavior of the atoms with the time of flight. This could be due to an unexpected change of the magnetic field and magnetic field gradients after switching off the coils, which would induce a shift of the zeeman-splitting for the imaging transition. Therefore we did the two dimensional TOF vs. imaging laser de-tuning and atom number scan shown in the upper part of Fig.(5.2). We see atoms with an imaging beam high de-tuned from the imaging transition at low times of flight which corresponds to the assumption that the magnetic field and therefore the splitting is changing with time. The change of the magnetic field seems to follow a decay with an overlaid oscillatory behavior. One explanation could be eddy currents resulting from the quick switch off of the magnetic field which are known to produce this vanishing phenomenon in the beginning of the TOF measurement [35]. Another possibility is that we have a

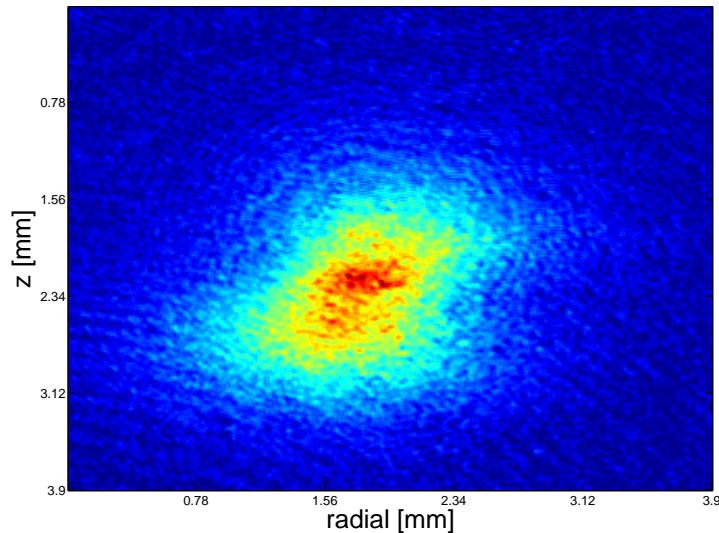


Figure 5.1.: Absorption image of $1.00 \pm 0.07 \times 10^7$ atoms imaged in situ in the quadrupole trap after holding them for 50 ms. The shape of the cloud resembles the quadrupole trap potential.

different shut down characteristic in V8 and V9 which could lead to instability of the system.

At first we followed the theory that we were inducing eddy currents in the copper parts of the coil mounting. Although we sliced all copper parts like the coil mountings while manufacturing to prevent big closed surfaces which are predestinated for eddy currents, it is of course not possible to get rid of all areas where eddy currents can be induced. The conductance of the used high purity copper (A.1.1) is also in the order of 100 [11] higher for a temperature of around 5 K compared to room temperature, which favors the appearance of eddy currents. If we induce arbitrary oriented eddy currents in the copper part which appear in copper parts of different geometry and have therefore different decay times, there would result a magnetic field which changes magnitude and orientation until all eddy currents have decayed. This magnetic field would shift the Zeeman-levels of the atoms, and the shifts would be position dependent. This could be an explanation why we see atoms at a strong de-tuning, but even then not as much as we can measure later at zero de-tuning. However, this can not explain the oscillations in atom number.

To explain the oscillations we measured the induction voltage in V7 during and after the switch off process. We observed an oscillation coincident to the oscillation in atom number. These measurements are presented in detail in [19]. The measured oscillation results from the behavior of the coils as a RLC-circuit.

Taking eddy currents and the RLC-circuit-behavior into account we can describe the measured data in a phenomenological manner. For further investigation of the

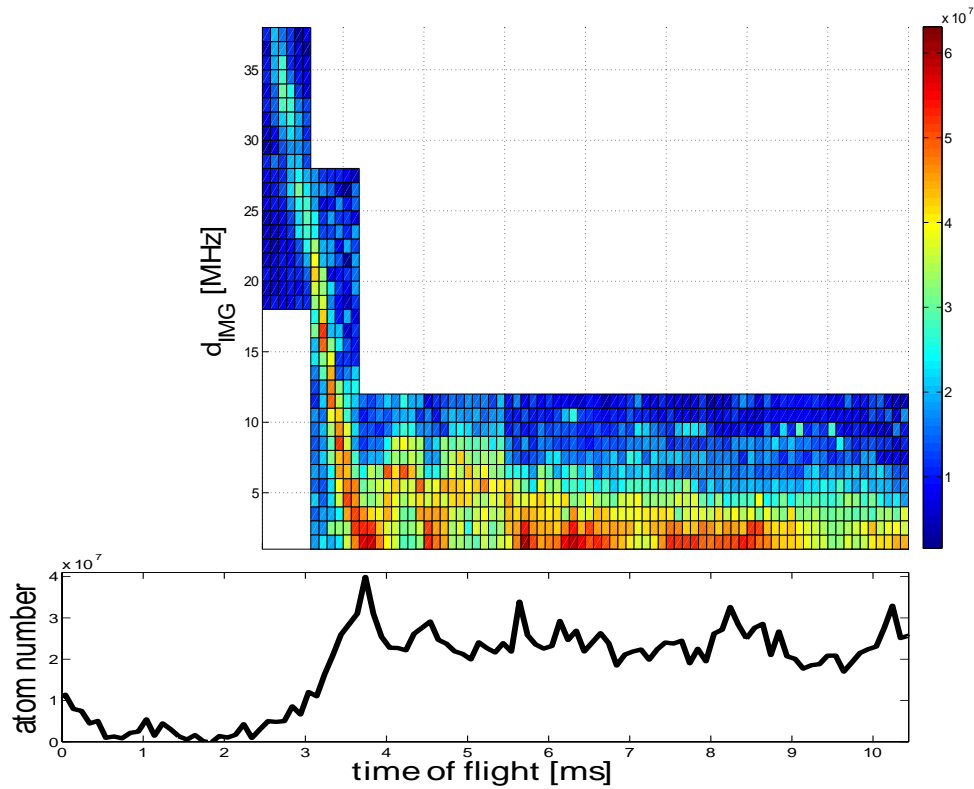


Figure 5.2.: The measured atom number in dependence of the time of flight. When imaging with zero detuning we observed a drop in atom number to effectively zero when increasing the time of flight. With rising the time of flight further the atoms came back and an oscillation in atom number could be observed (lower graph). With a imaging light detuning of around 35 MHz we were able to see atoms at a lower time of flight again. A two dimensional scan showed that the atoms are far detuned from resonance in the first 3 ms of the time of flight and that the detuning oscillates with the time of flight. (upper graph).

transport efficiency and optimization of the atom number we chose a TOF of 5.3 ms (which is a physical time of flight of 3.74 ms) to image the maximum atom number possible. A picture of such a measurement is shown in Fig.(5.3). The atom cloud has now a gaussian profile because the atoms had time to expand and reshape. It is about 3.3×3.3 mm in size and we measured an average atom number of $N_{av} = 4.73 \pm 0.17 \times 10^7$. The imaging beam for the imaging inside the cryostat has elliptical polarisation instead of the ideal case of circular polarisation, therefore this measured atom number can be improved by optimizing the polarity of the imaging beam.

Lifetime investigations

Another important parameter for further experiments in the cryostat is the lifetime of the ^{87}Rb atoms in the magnetic trap. In a simple decay rate model for a magnetic

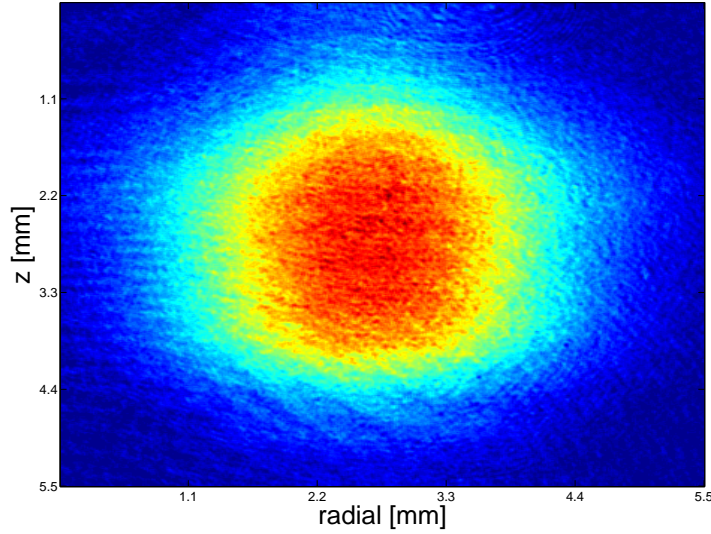


Figure 5.3.: Absorption image of $4.73 \pm 0.17 \times 10^7$ atoms after 5.3 ms time of flight. The atoms have reshaped to a spherical distribution according to their initial isotropic velocity distribution.

trap one finds Eq.(5.1) for the decrease of the atom number [14].

$$\frac{dN}{dt} = -\frac{N}{\tau} \quad (5.1)$$

The lifetime τ depends on loss processes which are independent from the atom number N . These are collisional processes with atoms of the background gas, absorption of background light or non-adiabatic transitions. We can therefore describe the decrease as exponential function.

$$N = N_0 e^{-\frac{t}{\tau}} \quad (5.2)$$

Therefore, the atom number depends only on the lifetime τ . The most important influence on the lifetime is the background pressure. Other influences could be background- or stray- light which kicks the atoms out of the trap or an instability of the trap potential and geometry. We can measure the lifetime by increasing the holding time in the magnetic trap, measuring a $N(t_{trap})$ curve and fitting the exponential function Eq.(5.2) to the measurement points.

We want to have the possibility to change the trap geometry to load into an quadrupole loffe trap or onto an atom-chip, which can't be accomplished arbitrarily fast. Additionally, we want to have the possibility to cool the atoms further and eventually reach Bose-Einstein-condensation by evaporative RF-cooling. For our calculated trap frequencies in the QuIC trap of $2\pi \times 20$ Hz and $2\pi \times 500$ Hz we have to drive a RF ramp with a ramp time up to 30 s [15]. Therefore we need a lifetime long enough to accomplish this with an adequate atom number.

Fig.(5.4) shows three different lifetime measurements in the magnetic trap. When we did first measurements we found a lifetime of only 4 to 7 s, like for the red data in Fig.(5.4). This may have been due to a bad pressure in the 4 K chamber. The pressure in the outer chamber of the cryostat was at about 3×10^{-9} mbar. We assumed a pressure in the order of 10^{-11} mbar inside the coil cage, resulting of the pumping effect of the 4 K cryopump but there is no possibility to measure the pressure directly in an cryogenic environment. We came up with several measures to lower the pressure inside. When we built in the Ioffe, Super-Ioffe and RF-coil as shown in Section 4.4.4, we also built in little aluminium containers filled with charcoal as shown in Fig.(4.26b). Charcoal can be used as cryosorption pump below a temperature of 10 K [21] and adsorbs He atoms of the background gas (all other gas atoms freeze out on the cold surfaces at this temperature). We used it as pellets¹ to maximize the pumping surface and installed 3 containers with an overall volume of $\approx 42.2 \text{ cm}^3$ on the 4 K base.

Another possibility for a bad pressure was that the shield has 20 drilled holes with about 1 cm diameter in the upper part. These holes are there for improving the pumping speed when evacuating the chamber from room pressure by the rotary vane pump and the TMP. While planning of the shield design there was the concern that pumping the cryo chamber would take too long without an upper connection of the inner cryo chamber with the outer chamber and the valve where the pumps are connected. Since we only had a pressure of 3×10^{-9} mbar in the outside chamber it was possible that this relatively high pressure would also affect the inner pressure through this connections. Therefore we closed 18 holes, leaving only 2 open.

After closing the holes and mounting the charcoal containers on the 4 K-base we did another lifetime measurement and observed a little improvement to 13.7 s (black curve in Fig.(5.4)). This is better than the measurements before, but still not satisfying for our purpose. When closing the valve connecting cryo chamber and pumps we noticed a drop in the outer pressure from 3×10^{-9} mbar to 5×10^{-10} mbar. This leads to the conclusion that we have a better pump power of the cold surfaces, especially of the 70 K shield than by pumping with the TMP.

There was also the concern that the electronics of the Gifford-McMahon coldfinger could produce noise which would result in an unstable trap potential. This could be ruled out by switching off the cryofinger via a TTL signal during measurement, which had no effect.

In a subsequent measurement the lifetime improved to 168.7 s (blue curve in Fig.(5.4)) and this high value was reproduceable ever since. Although there is no direct causal connection to our taken measures, we assume that all of them lead to this improvement and solved the issue. Therefore further steps like loading in the quadrupole-Ioffe trap and evaporative RF-cooling can be approached.

¹Carl Roth Aktivkohle, $\sim 3 \text{ mm}$, dampfaktiviert

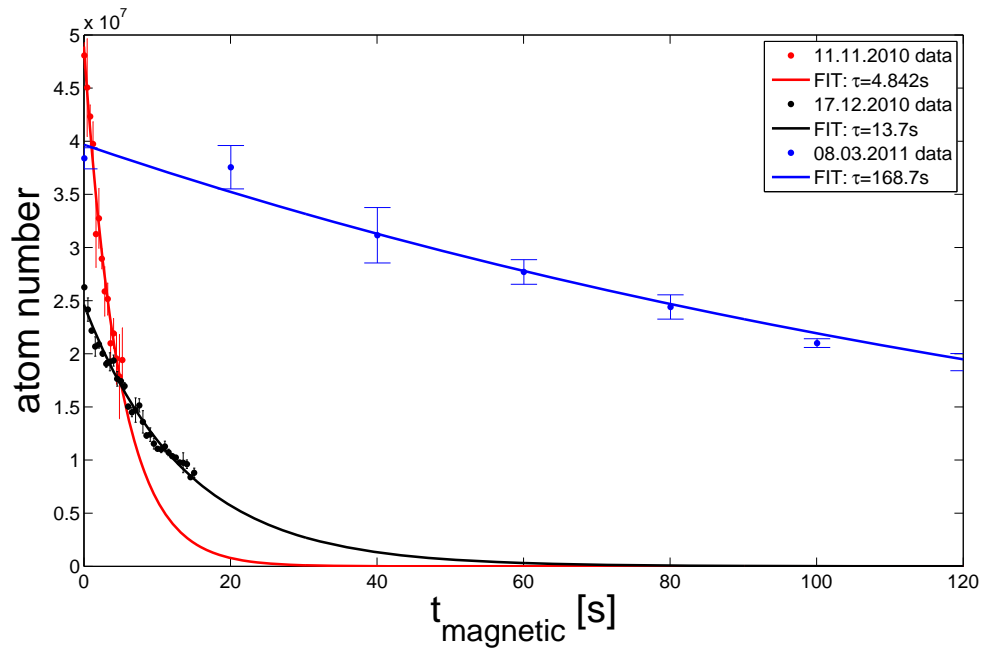


Figure 5.4.: The improvement in the achieved lifetime τ in the quadrupole trap.

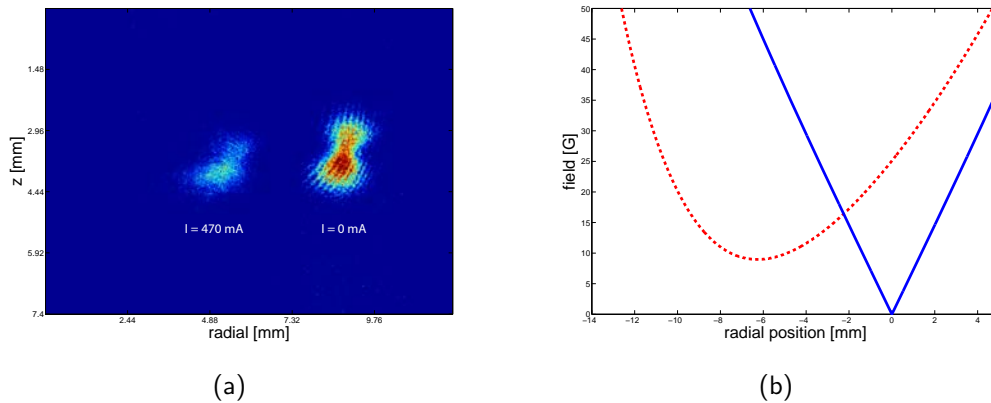


Figure 5.5.: (a) First picture of atoms in the QulC trap. This is a collage of two measurements to illustrate the difference between one measurement inside the quadrupole trap ($I_{Ioffe} = 0$ mA) and one in a QulC trap ($I_{Ioffe} = 470$ mA). The trap position moves in direction of the loffe-coil. (b) The calculated change of the radial potential for the measurements in (a).

5.2. Atoms in the quadrupole-loffe-trap

After building the loffe coil into the cryostat we started first attempts to load the atoms into a Quadrupole-loffe (QulC) trap configuration. We trapped the atoms first in the superconducting quadrupole trap as shown in the last section and ramped then the current in the loffe coil up. Fig.(5.5) shows the measurement in the quadrupole trap ($I_{Ioffe} = 0$ mA) and in a first quadrupole-loffe trap ($I_{Ioffe} = 470$ mA). A simulation analog to the calculations in Section 3.4 is shown in Fig.(5.5b). According to this the QulC trap has a high trap bottom of about 9 G and the harmonic trap potential is very broad (red dashed line). This is in good agreement with Fig.(5.5) where the cloud has a big spatial distribution. To have a good starting condition for cooling to a BEC we want to have a narrower trap and a smaller atom cloud. First simulations show that we can reach this with a higher current in the quadrupole coils.

6. Conclusion and future prospects

This thesis has been carried out during the build up phase of the vertical magnetic transport and the cryostat. The MOT optics was built new, the previously built horizontal transport was moved, the superconducting transport coils were designed and manufactured, the experimental control program was modified and adapted, first atoms were measured in the cryostat, the MOT and transport were optimized, the trapped atoms in the cryostat were characterized and first measurements of atoms in the superconducting quadrupole-loffe trap were presented. We were able to transport more than 7×10^7 atoms into the cryostat and measured a lifetime exceeding 230 s.

First qualitative estimations for the lifetime of atoms in the QuIC trap show that it is in the order of 15 s which is too low to attempt Bose-Einstein-condensation. A reason for this could be instabilities in the coil currents due to electronic noise. Since all coils are driven separately by a current source in the primary setup, such noise would change the trap geometry, heat the atoms and allow them to escape. Therefore the coils should be driven in series to have the same noise pattern on every coil. Possibilities to do this would be with a power splitter which splits up the currents to V8, V9 and the loffe-coil. A difficulty with this solution would be that the transport current curves have to be implemented in the splitter ratio between V8 and V9, therefore we would have to be able to control the splitting amount fast and accurate. Another approach for this would be to use the BIAS coils shown in Fig.(4.22) for a buffer trap, that means loading the atoms from the separately driven quadrupole trap (V8/V9) into another quadrupole trap done by the grey BIAS coils, then switch V8 and V9 and the loffe-coil on a serial circuit (while the current is zero) and finally load in the serial QuIC trap. This would solve the problem that we can't switch directly to a serial circuit while the current is up because we would get peaks due to the high inductance of the coil which would destroy the trap and we would also don't need to control any splitting voltage which is an additional error source.

The ordered mounting for a superconducting atom-chip (Fig.(6.1)) will be made out of quartz (SiO_2), which is an electrical insulator but has at the same time a very good thermal conductivity ($185 \text{ W}/(\text{m} \times \text{K})$ at 4 K) [11]. Atom-chips made from sapphire (Al_2O_3) which is even a better thermal conductor ($600 \text{ W}/(\text{m} \times \text{K})$ at 6 K) with different diameters of Niobium Z-wires ($200 \mu\text{m}$, $400 \mu\text{m}$, ...) to test the critical currents of the Z-wires are manufactured and will be ready to build in when the sapphire-mounting will arrive.

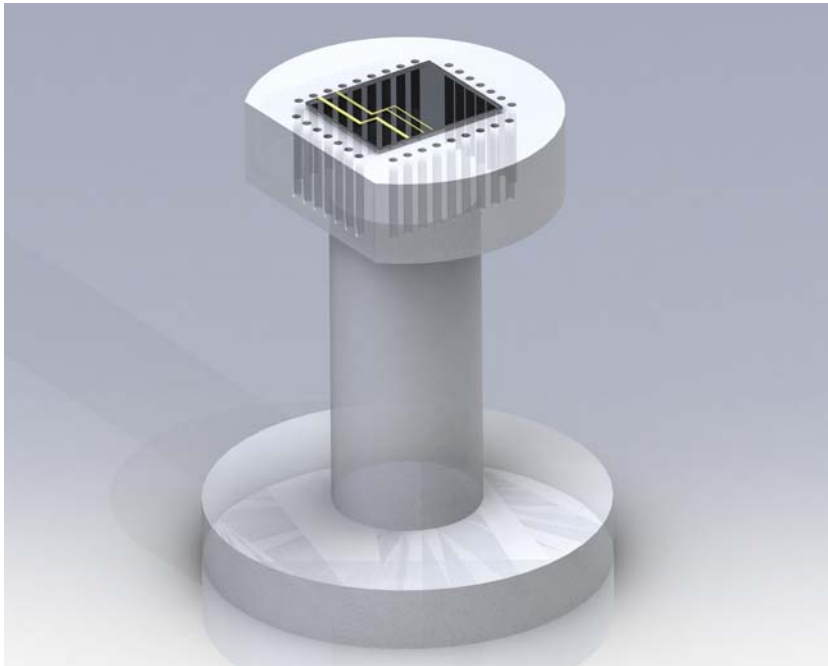


Figure 6.1.: A rendered image of the chip-mounting and the planned atom chip design. The mounting is made of quartz (SiO_2) and provides 32 drilled holes for the wiring. The atom chip will be mounted on top. The chip material will be sapphire (Al_2O_3) and the superconducting chip wires will be made out of Niobium. The mounting will be clamped on the 4 K-base and positioned in the superconducting trap center as sketched in Fig.(4.22).

In conclusion the accomplishments of transporting atoms into the cryostat clear the way for several exciting experiments with atoms in a cryogenic environment. Additionally to the quantum interconnect experiment explained in this thesis it gives the possibility to analyze the interaction of ultra-cold atoms with superconducting surfaces and structures.

A. Appendix

A.1. Properties of cryogenic materials

A.1.1. High purity copper

Facts about the high purity copper used for base and coilmountings, Data taken from [10, 11]:

- Classification:
Europe/International (EN/ISO): Cu-HCP (old: SE-Cu 2.0070)
US (ASTM/UNS): C10300/C10800
- Properties:
Purity: $\geq 99.95\%$, oxydized with 0.002 to 0.007 % Phosphor
Bi: 0.0005 % , Pb: 0.005 %
sum of all elements additional to copper (As, Bi, Cd, Co, Cr, Fe, Mn, Ni, O, Pb, S, Sb, Se, Si, Sn, Te, Zn): 0.03 %
 $RRR = \frac{\rho_{293K}}{\rho_{4K}} = 50 - 700$ (depends on the grade of oxidation)
- Supplier:
Schiekmetall Handels-GmbH, Albert Schweitzer-Gasse 9, A-1140 Wien,
<http://www.schiekmetall.at>

Facts about the high purity copper used for the rods of the coilcage, Data taken from [18]:

- Classification:
Cu-OFHC, CV007960
- Properties:
Purity: $\geq 99.95\%$
Additional elements in ppm:
Ag 100, Al 1, Bi 1, Ca 3, Cd 1, Fe 2, Mg 1, Pb 3, Si 2, Sn 2.

- Supplier:

Goodfellow GmbH, Postfach 13 43, D-61213 Bad Nauheim, Germany,
<http://www.goodfellow.com/>

A.1.2. Superconducting wire

Facts about the superconducting wire used all superconducting coils inside the cryostat, Data taken from [23]:

- Classification:

54S43, AWG 36 (0.127 mm diameter)

Serial No. 378E-98B3B2A

- Properties:

Copper matrix with 54 NbTi filaments (9 μm filament diameter), with a Cu:NbTi ratio of 1.3:1

FORMVAR¹ insulation

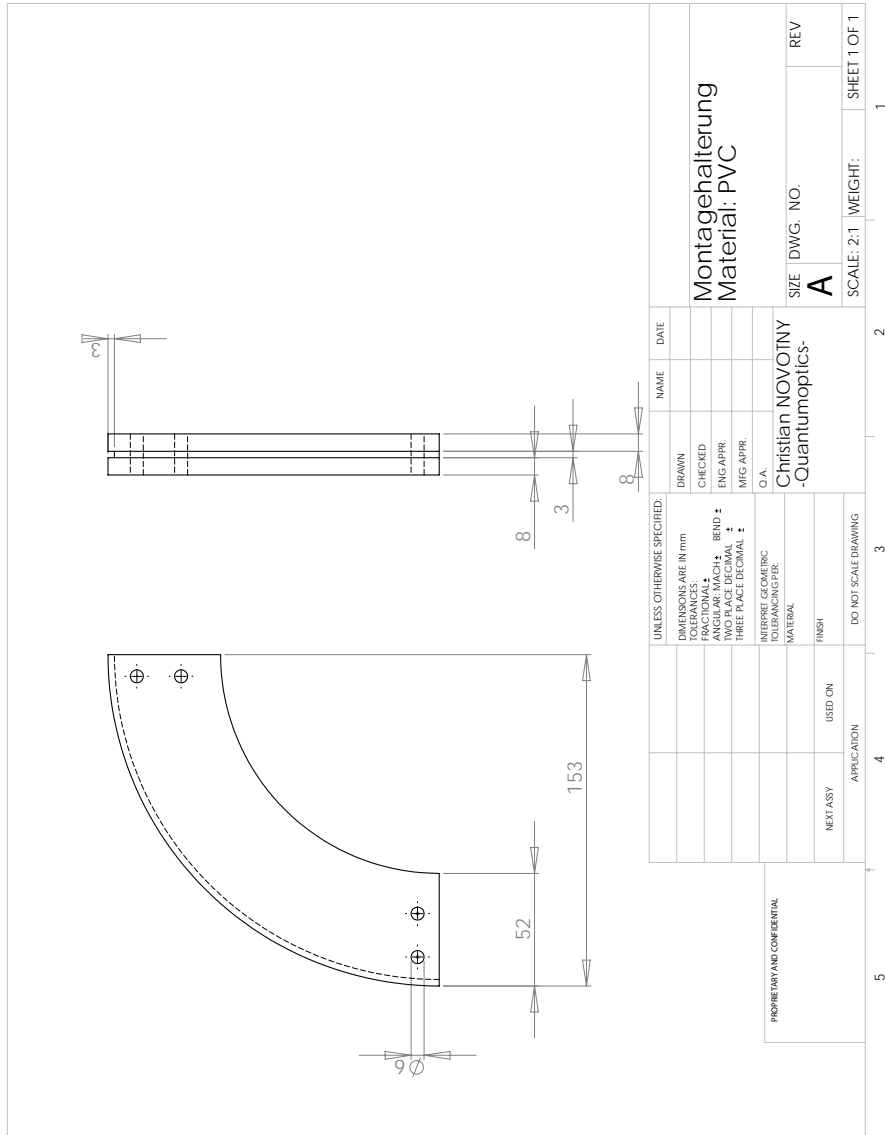
Superconducting below the $T_C = 9.2$ K of NbTi

- Supplier:

Supercon Inc. 830 Boston Turnpike, Shrewsbury, MA 01545,
<http://www.supercon-wire.com/>

¹Essex FORMVAR, Essex Group, Inc. 1601 Wall Street, Fort Wayne, IN 46802,
www.superioressex.com

A.2. Construction plans for the cryo-compensation-coil-mountings



B. Acknowledgements

I'd like to thank ...

- Prof.Dr. Jörg Schmiedmayer for giving me the opportunity to work on an exciting and ambitious project and for opening new levels of understanding to me.
- Dr. Stephan Schneider for supervising my work and supporting me with all obstacles encountered during this thesis.
- Dr. Stefan Haslinger for showing me how to organize a big project and never lose the overview, no matter how confusing things seem to be and for mentoring me in the beginning of this thesis.
- Dr. Christoph "Sensei" Hufnagel, for showing me how to master the apparatus with magic hands and always providing a diverse mix of music in the lab.
- DI Stefan Minniberger and MSc. Fritz Diorico for all the fun while trapped in the "QuIC-trap", may it never open again!!
- Dr. Hannes Majer and all other scientists of the QuIC team and the AtomChip group for a productive and congenial working environment and all the fun attached.
- DI Christoph Gösselsberger, for all the more or less physical activities spent together since the very beginning of our studies.
- MSc. Patrick "Master P" Moser, for all the amazing creative nights and seething electronic sound!!!
- all my friends who went along with me during my studies, for all the good times and the wild student life.
- my best friend Mag. Claudia Leithner, for being always there and ready for a long and fruitful discussion to uncover new views and insights.
- my sister Katharina Novotny who was always there for me when something didn't work out too well.
- and finally my mother, Elfriede Novotny, for all her unconditioned loving support and kind understanding throughout my studies.

Bibliography

- [1] Md. Manirul Ali, Dipankar Home, A. S. Majumdar, and Alok K. Pan. Quantum time-of-flight distribution for cold trapped atoms. *Phys. Rev. A*, 75(4):042110, Apr 2007.
- [2] R. Amsüss. Development of a source of ultracold atoms for cryogenic environments. Master's thesis, Technische Universität Wien, Atominstitut, 2008.
- [3] R. Amsüss, C. Koller, T. Nöbauer, S. Putz, S. Rotter, K. Sandner, S. Schneider, M. Schramböck, G. Steinhauser, H. Ritsch, J. Schmiedmayer, and J. Majer. Cavity QED with magnetically coupled collective spin states. *arXiv:1103.1045v1*, 2011.
- [4] P. B. Antohi, D. Schuster, G. M. Akselrod, J. Labaziewicz, Y. Ge, Z. Lin, W. S. Bakr, and I. L. Chuang. Cryogenic ion trapping systems with surface-electrode traps. *Review of Scientific Instruments*, 80(1):013103, 2009.
- [5] S. Bartalini, I. Herrera, L. Consolino, L. Pappalardo, N. Marino, G. D'Arrigo, and F.S. Cataliotti. Full characterization of the loading of a magneto-optical trap from an alkali metal dispenser. *The European Physical Journal D*, 36:101–104, 2005.
- [6] P. Berman, editor. *Cavity quantum electrodynamics*. Adv. At. Mol. Opt. Phys. Academic Press, New York, 1994.
- [7] M. Brajdic. Entwicklung einer Computersteuerung und ihre Anwendung in einem Experiment zur vereinfachten Bose-Einstein Kondensation in einer Oberflächenfalle. Diploma thesis, University of Heidelberg, 2003.
- [8] J. Dalibard and C. Cohen-Tannoudji. Laser cooling below the Doppler limit by polarization gradients, simple theoretical models. *J. Opt. Soc. Am. B*, 6:2023, 1989.
- [9] K. B. Davis, M.-O. Mewes, M. R. Andrews, N. J. van Druten, D. S. Durfee, D. M. Kurn, and W. Ketterle. Bose Einstein condensation in a gas of Sodium atoms. *Phys. Rev. Lett.*, 75:3969, 1995.
- [10] Deutsches Kupferinstitut. *SE-Cu_Cu-HCP.pdf*, 2005. Werkstoff-Datenblatt.

- [11] Jack W. Ekin. *Experimental techniques for low-temperature measurements. Cryostat design, material properties and superconducting critical current testing*. Oxford University Press, 2006.
- [12] B. Engeser. *Optische Abbildung einer atomaren Dichteverteilung*. Diploma thesis, Universität Heidelberg, 2002.
- [13] T. Esslinger, I. Bloch, and T. W. Hänsch. Bose-einstein condensation in a quadrupole-ioffe-configuration trap. *Phys. Rev. A*, 58:R2664–R2667, 1998.
- [14] David Fagnan. Study of collision cross section of ultra-cold Rubidium using a magneto-optic and pure magnetic trap. Master's thesis, THE UNIVERSITY OF BRITISH COLUMBIA, 2009.
- [15] C. J. Foot. *Atomic Physics*. Oxford University Press, 2005.
- [16] A. Frisch. Magnetischer transport ultrakalter rb-atome und flugzeit-massenspektrometrie im barbi-experiment. Master's thesis, Leopold-Franzens Universität Innsbruck, 2009.
- [17] SAES getters. Alkali metal dispensers. Technical report, SAES, 2007. www.saesgetters.com.
- [18] Goodfellow GmbH. <http://www.goodfellow.com/catalogue>.
- [19] Stefan Haslinger. *Cold Atoms in a Cryogenic Environment*. PhD thesis, Technische Universität Wien, 2011.
- [20] E. Hecht. *Optics*. Addison-Wesley, Reading, 1989.
- [21] H. Hseuh, T. Chou, H. Worwetz, and H. Halama. Cryosorption pumping of He by charcoal and a compound cryopump design for TSTA. *Symposium on Engineering Problems of Fusion Research*, 3, 1979.
- [22] Christoph Hufnagel. *Superconducting microchips for ultracold atoms*. PhD thesis, Technische Universität Wien, 2011.
- [23] Supercon Inc. http://www.supercon-wire.com/products_fine_sc_wires.html.
- [24] W. Ketterle, D.S. Durfee, and D.M. Stamper-Kurn. Making, probing and understanding bose-einstein condensates. *arXiv:cond-mat/9904034v2*, 2:87, 1999.
- [25] P. Krüger and J. Schmiedmayer. Atomchips: Integrated circuits for matter wave manipulation. *Contemp. Phys.*, 2004. In preparation.
- [26] K. Lindquist, M. Stephens, and C. Wieman. Experimental and theoretical study of the vapor-cell zeeman optical trap. *Phys. Rev. A*, 46(7):4082–4090, Oct 1992.

- [27] N. Lippok. A magnetic transport for ultracold atoms. Master's thesis, Ruperto-Carola University of Heidelberg, 2008.
- [28] Dieter Meschede. *Optik, Licht und Laser*. Vieweg Verlag, 2008.
- [29] H. J. Metcalf. *Laser Cooling and Trapping*. Springer Verlag, Heidelberg Berlin New York, 1999.
- [30] C. Monroe, W. Swann, H. Robinson, and C. Wieman. Very cold trapped atoms in a vapor cell. *Phys. Rev. Lett.*, 65:1571, 1990.
- [31] T. Pellizzari, S. A. Gardiner, and P. Zoller. Decoherence, continuous observation, and quantum computing: A cavity QED model. *Phys. Rev. Lett.*, 75:3788, 1995.
- [32] D. Petrosyan, G. Bensky, G. Kurizki, I. Mazets, J. Majer, and J. Schmiedmayer. Reversible state transfer between superconducting qubits and atomic ensembles. *Phys. Rev. A*, 79:040304(R), 2009.
- [33] W. Rohringer. *Stochastic Optimization in an Ultracold Atom Experiment*. Diploma thesis, TU Wien, 2008.
- [34] J. Schmiedmayer. Guiding and trapping a neutral atom on a wire. *Phys. Rev. A*, 52:R13, 1995.
- [35] S. Schneider. *Bose-Einstein Kondensation in einer magnetischen Z-Falle*. PhD thesis, Universität Heidelberg, 2003.
- [36] R. J. Schoelkopf and S. M. Girvin. Wiring up quantum systems. *Nature*, 451:664–669, 2008.
- [37] A. M. Steane. Quantum computing. *Rep. Prog. Phys.*, 61:117, 1998.
- [38] D. A. Steck. Rubidium 87 D line data. Technical report, Oregon Center for Optics and Department of Physics, University of Oregon, 2008.
- [39] John E. Traister and Ronald T. Murray. *Commercial Electrical Wiring*. Craftsman Book Company, 1994.
- [40] J. Verdu, H. Zoubi, Ch. Koller, J. Majer, H. Ritsch, and J. Schmiedmayer. Strong magnetic coupling of an ultracold gas to a superconducting waveguide cavity. *Phys. Rev. Lett.*, 103:436, 2009.
- [41] M. Wilzbach. *Single atom detection on an atom chip with integrated optics*. PhD thesis, Ruperto-Carola University of Heidelberg, 2007.
- [42] W. H. Wing. On neutral particle trapping in quasistatic electromagnetic fields. *Prog. Quant. Electr.*, 8:181, 1984.